

Comparing intrarift and border fault structure in the Malawi Rift: Implications for normal fault growth

Manon Carpenter^{a,*}, Jack N. Williams^{a,**}, Åke Fagereng^a, Luke N.J. Wedmore^b, Juliet Biggs^b, Felix Mphemo^c, Hassan Mdala^c, Zuze Dulanya^d, Blackwell Manda^d

^a School of Earth and Environmental Sciences, Cardiff University, UK

^b School of Earth Sciences, University of Bristol, UK

^c Geological Survey Department, Mzuzu Regional Office, Mzuzu, Malawi

^d Geography and Earth Sciences Department, University of Malawi, Zomba, Malawi

ARTICLE INFO

Keywords:

Malawi Rift
Fault zone structure
Normal faults
Continental rifts
Microstructures

ABSTRACT

Early stages of normal fault growth are seldom described using field observations of active normal faults. Here we first estimate the displacements of active border and intrarift faults in the Zomba Graben in the low extension (< 10 %) Malawi Rift, and then quantify micro-to macroscale fault damage and mineralisation associated with their surface exposures. The 22 km long Mlunguzi and 39 km long Chingale Step intrarift faults have fault zones 4–52 m wide. In contrast, we estimate the fault zone of the 51 km long Zomba border fault is 32–118 m wide. Calcite and clay alteration is limited to the fault damage zones and fault cores, and the extent and intensity of fault damage and mineral alteration is greater on the Zomba border fault compared to the intrarift faults. Relative to global compilations, normal faults in the Zomba Graben have lengthened quickly while developing narrow fault zones, given their displacement. The minor damage on these long, low-displacement normal faults may reflect the influence of lithology, negligible fault healing, and/or activation of pre-existing weaknesses.

1. Introduction

Our understanding of brittle deformation in the Earth's crust requires reconciling predictions from mechanical models of fracture propagation and growth with field and laboratory observations of fault structure (e.g., Cowie and Scholz, 1992; Faulkner et al., 2011; Stanton-Yonge et al., 2020). One way of testing these predictions is to compare empirical and theoretical scaling relationships between fault displacement and length (Walsh and Watterson, 1988; Walsh et al., 2002; Kim and Sanderson, 2005; Torabi and Berg, 2011; Rotevatn et al., 2019; Lathrop et al., 2022), or between fault displacement and the combined width of fault core and damage zone (henceforth referred to as fault zone width, Fig. 1; e.g., Cowie and Scholz, 1992; Anders and Wiltshcko, 1994; Shipton and Cowie, 2003; Shipton et al., 2006; Savage and Brodsky, 2011; Faulkner et al., 2011; Choi et al., 2016; Torabi et al., 2020).

As cumulative displacement along normal faults is inherently preserved in the geologic record, our empirical understanding of how this type of fault grows is best constrained relative to other types of faults

(see recent review by Lathrop et al., 2022). From these data, it is now generally established that normal faults follow a two-stage 'hybrid' growth model in displacement-length space, whereby faults lengthen rapidly during their early stages of displacement accrual, and this is followed by a period of increasing cumulative displacement with little fault lengthening (Walsh et al., 2002; Rotevatn et al., 2019; Lathrop et al., 2022). Fault displacement-fault zone width scaling relationships also suggest a two-stage growth model, with a possible break in the fault zone width-displacement power-law distribution when displacement reaches ~ 100–200 m (Savage and Brodsky, 2011; Torabi et al., 2020). However, there is considerable scatter within both displacement-length and displacement-width datasets when faults of all lithologies, maturities and tectonic histories are combined (Torabi et al., 2020; Lathrop et al., 2022). Furthermore, a number of key questions remain about normal fault growth: (1) the inter-relationships between normal fault length, displacement, and width (Childs et al., 2009), (2) the role of lithology and pre-existing crustal weakness (e.g., Philippon et al., 2015; Williams et al., 2022a), (3) how models for the growth of individual

* Corresponding author. School of Earth and Environment, University of Leeds, UK.

** Corresponding author. Department of Geology, University of Otago, New Zealand.

E-mail addresses: eemrca@leeds.ac.uk (M. Carpenter), jack.williams@otago.ac.nz (J.N. Williams).

<https://doi.org/10.1016/j.jsg.2022.104761>

Received 11 May 2022; Received in revised form 7 November 2022; Accepted 15 November 2022

Available online 16 November 2022

0191-8141/© 2022 The Authors. Published by Elsevier Ltd. This is an open access article under the CC BY license (<http://creativecommons.org/licenses/by/4.0/>).

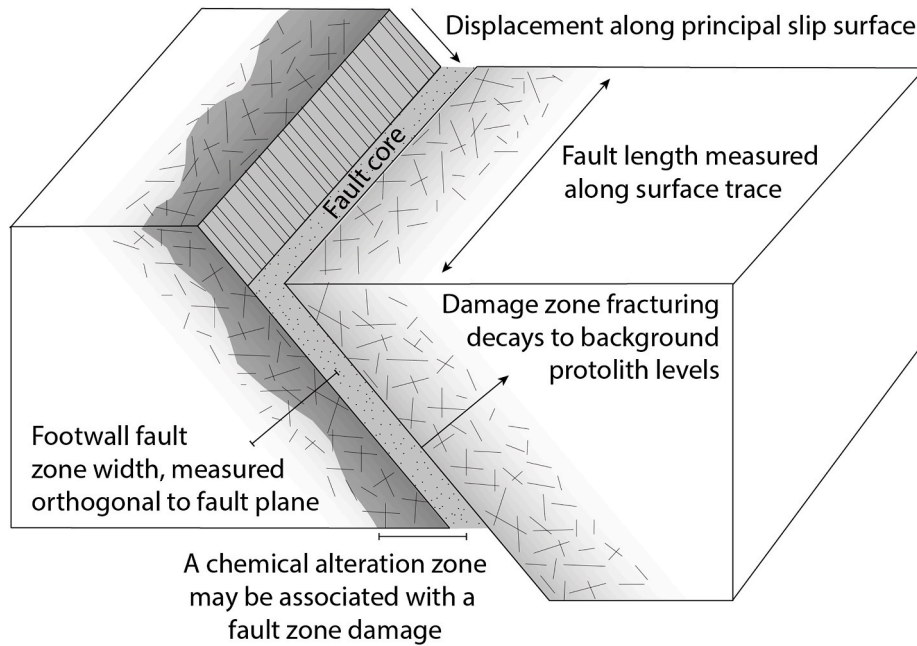


Fig. 1. Schematic diagram of a geometrically simple normal fault, hosted in crystalline rock. Displacement is localised on a principal slip surface within the fault core, and damage zone fracturing decays to background protolith levels. A chemical alteration zone may be associated with fault zone damage. Hanging wall and footwall fault zones and chemical alteration zones need not be symmetrical. Modified from [Torabi and Berg \(2011\)](#).

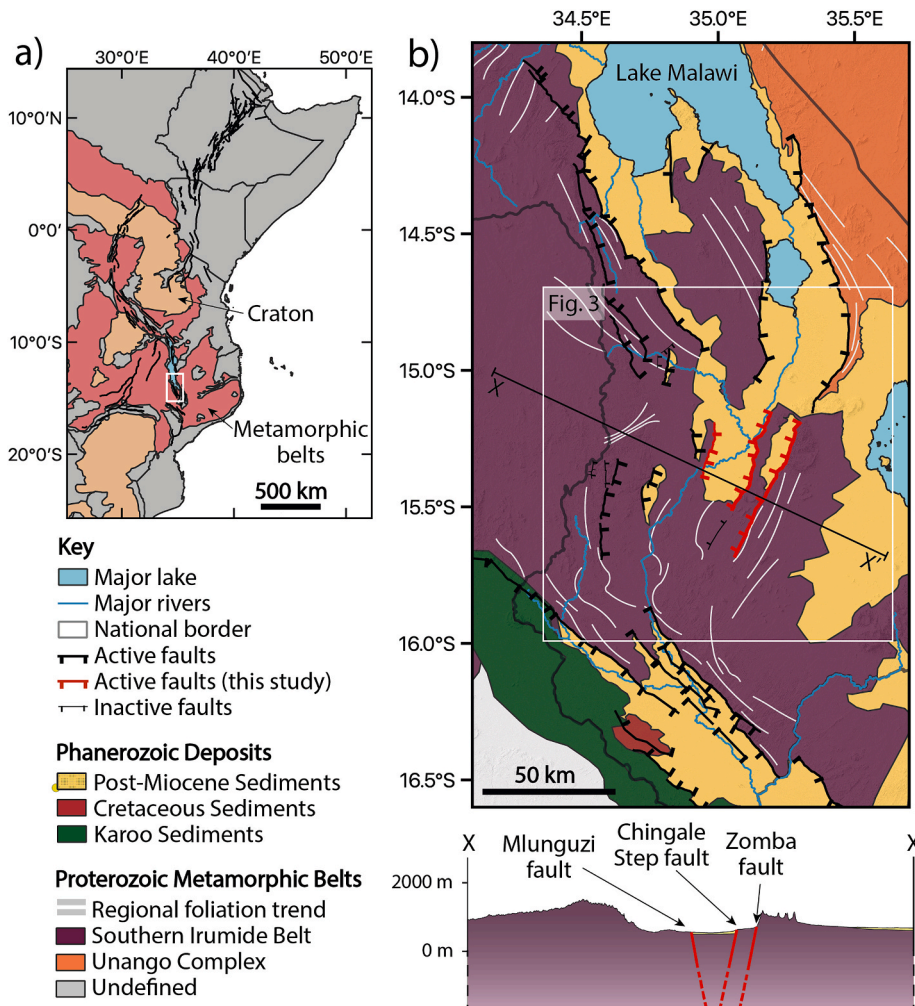


Fig. 2. a) Location of Fig. 2b (white box) within East Africa. Major East African Rift structures are displayed alongside cratons (orange) and mobile belts (red). b) Geological map of southern Malawi Rift with Proterozoic units after [Fritz et al. \(2013\)](#). Foliation trends are collated from SRTM images, field measurements and previous studies ([Bloomfield, 1958, 1965](#); [Habgood, 1963](#); [Bloomfield and Garson, 1965](#); [Walshaw, 1965](#); [Dawson and Kirkpatrick, 1968](#); [Hodge et al., 2018](#); [Williams et al., 2019](#)). White box locates the Zomba Graben, which is shown in Fig. 3. (For interpretation of the references to colour in this figure legend, the reader is referred to the Web version of this article.)

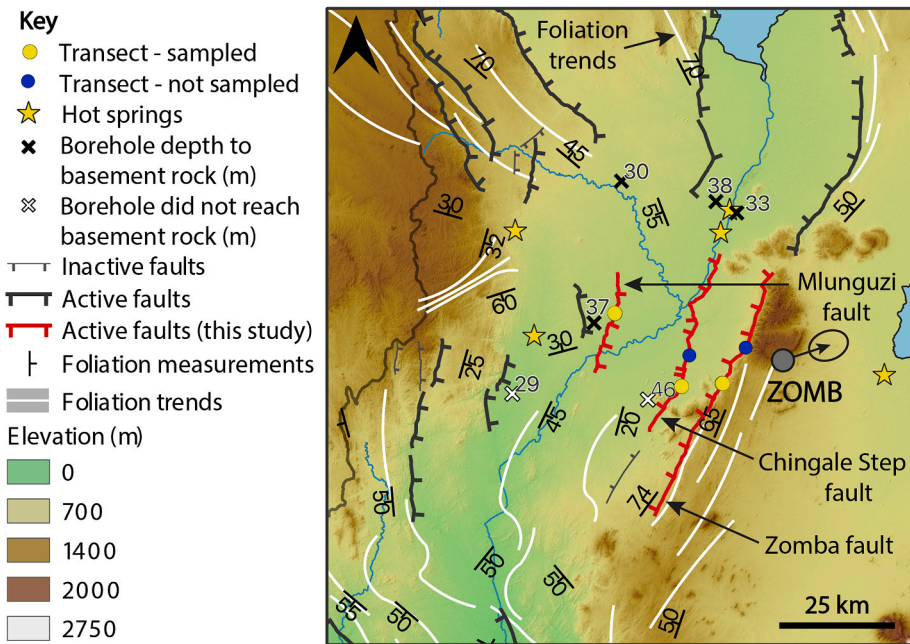


Fig. 3. The Zomba Graben, as highlighted in Fig. 2b, with Mlunguzi, Chingale Step and Zomba faults highlighted in red. Borehole depths are displayed according to whether or not basement rock was reached (Bloomfield, 1965; Bloomfield and Garson, 1965; Walshaw, 1965), and the GPS vector relative to the stable Nubian plate is shown (ZOMB; Stamps et al., 2018). Transect samples are taken where each fault is relatively straight. (For interpretation of the references to colour in this figure legend, the reader is referred to the Web version of this article.)

normal faults are reflected in the evolution of crustal-scale extension (Pan et al., 2022), and (4) a single fracture mechanics model that can reconcile the empirical observations of fault length, displacement and width (Faulkner et al., 2011). Hence, there is an ongoing need to collect more outcrop data from fault zones that can help constrain how normal faults grow.

Long term normal fault growth analyses must also consider the short-term processes that operate around fault zones during individual seismic cycles (e.g., Chester et al., 1993; Wibberley and Shimamoto, 2003; Caine et al., 2010; Faulkner et al., 2010). In particular, the structural evolution of faults may be linked to fluid-rock interactions that can act to localise slip in fault zones through alteration-weakening of fault rocks (e.g., Wintsch et al., 1995; Wibberley and Shimamoto, 2003; Holdsworth et al., 2011; Boulton et al., 2012), or conversely result in the activation of new slip planes and the development of wide fault zones through fluid-rock interactions that result in cementation and embrittlement of the fault zone (Caine et al., 2010; Callahan et al., 2020). The lithology of the surrounding protolith and the fault's orientation with respect to the regional stress state may also influence how the ratio of displacement to fault zone width evolves (Faulkner et al., 2003; Fletcher et al., 2020).

In this study, we provide constraints for the displacement and fault zone width of three active, 22–51 km long, normal faults located within the Zomba Graben, near the southern-end of the Western Branch of the East African Rift System (Fig. 2). The studied faults include one relatively high displacement (745 ± 125 m) basin-bounding 'border' fault and two lower displacement (75–235 m) 'intra-rift' faults. Because displacement-length and displacement-width scaling are progressively developed features of fault zones (Rotevatn et al., 2019), these faults in the relatively low strain Zomba Graben provide an ideal opportunity to constrain fault scaling during the early period of fault displacement accumulation. Furthermore, there have been relatively few studies that have compared the structure of border and intra-rift faults from the same rift basin before, even though this rift-scale architecture is common throughout the well-studied East African Rift System (Ebinger, 1989; Karner et al., 2000; Accardo et al., 2018; Muirhead et al., 2019; Wedmore et al., 2020a; Wright et al., 2020), and is thought to play a key role in facilitating rifting in this region (Daly et al., 1989).

We first assess the distribution and intensity of damage and chemical alteration associated with each fault using field, microstructural, and compositional analyses to address the variation in fault zone structure

within the Zomba Graben. By placing our results in the context of global fault-scaling datasets, we then consider the crustal controls which may influence fault growth in the Malawi Rift. Our results can be used more broadly to investigate normal fault growth mechanisms, and the spatiotemporal evolution of continental rifts.

2. Geological setting

The Malawi Rift is an active, amagmatic segment of the East African Rift System (Fig. 2; Ebinger et al., 1987), hosted within ~ 35 – 45 km thick Proterozoic crust that is cold, anhydrous and seismogenic almost to the Moho (~ 35 – 45 km; Jackson and Blenkinsop, 1993; Nyblade and Langston, 1995; Yang and Chen, 2010; Fagereng, 2013; Ebinger et al., 2019; Njinju et al., 2019; Craig et al., 2021; Stevens et al., 2021; Sun et al., 2021). The Malawi Rift extends ~ 750 km from the Rungwe Volcanic Province, Tanzania, to southern Malawi, where it intersects the Karoo-reactivated Lower Shire Graben that connects it in the south to the Urema Graben in Mozambique (Habgood, 1963; Ebinger, 1989; Castaing, 1991; Ring and Betzler, 1995; Chorowicz, 2005; Laó-Dávila et al., 2015; Dulanya et al., 2017; 2022; Kolawole et al., 2021; Williams et al., 2022b). Campaign and continuous GPS measurements indicate the Malawi Rift is accommodating ENE-WSW ~ 0.5 – 1.5 mm/yr extension between the Rovuma and San plates (Wedmore et al., 2021). Low temperature thermochronology indicates that the onset of rifting in the Late Oligocene to Early Miocene (~ 23 Ma) was approximately coeval along the rift (Mortimer et al., 2016; Ojo et al., 2022b). However, total rift extension is higher in northern and central Malawi where faults have accumulated greater displacements and thicker syn-rift sediment packages (Accardo et al., 2018; Scholz et al., 2020). Hence, the 7–10 % total rift extension recorded in these basins (Scholz et al., 2020) provides an upper bound for rift extension in southern Malawi.

Like other segments of the East African Rift System, the Malawi Rift is expressed as a series of grabens and half grabens that are defined by segmented border faults (Ebinger et al., 1987; Flannery and Rosendahl, 1990; Laó-Dávila et al., 2015; Hodge et al., 2019; Scholz et al., 2020; Wedmore et al., 2020b). This study focusses on the Zomba Graben (Fig. 3), a NNE-SSW trending basin at the southern end of the Malawi Rift (Bloomfield, 1965; Dulanya et al., 2017; Wedmore et al., 2020a; Kolawole et al., 2021; Williams et al., 2021). The Proterozoic Southern Irumide Belt provides structurally complex basement rock in the Zomba

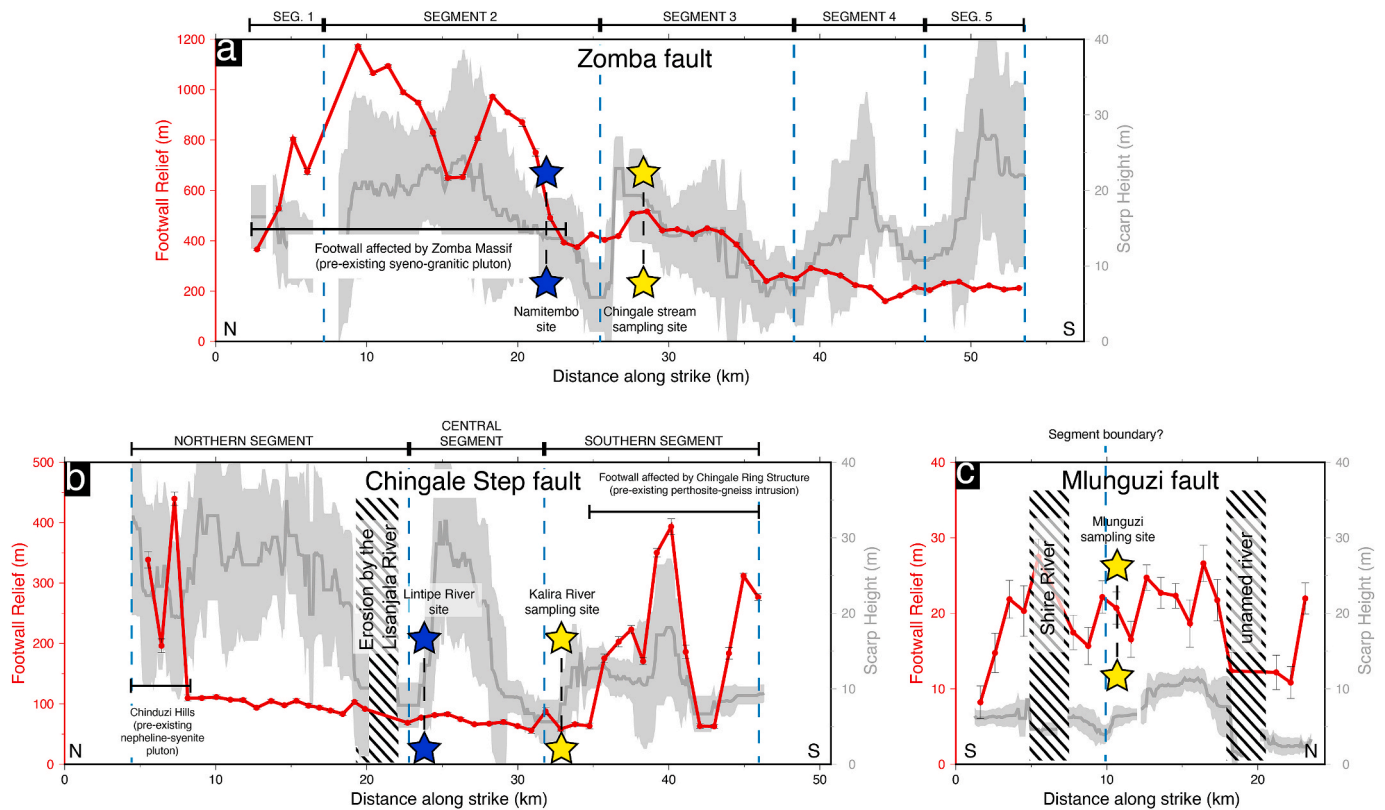


Fig. 4. Along-strike segmentation, footwall relief, scarp height and sampling locations along the three studied faults. Segmentation and scarp height measurements from [Wedmore et al. \(2020a\)](https://doi.org/10.5281/zenodo.3582282) (<https://doi.org/10.5281/zenodo.3582282>). Footwall relief was measured every 1 km along strike using stacked profiles of TanDEM-X topographic data that had been sampled every 100 m along strike. We measured the difference in elevation between the highest point on the footwall within 3 km of the fault surface trace, and the elevation of the fault itself. In areas where pre- and post-kinematic intrusions are present, these affect our measurements. Thus, we do not include these when estimating the throw of the faults.

Graben (Fig. 2), and has previously experienced amphibolite-granulite facies metamorphism during the gradual Proterozoic amalgamation of the African continent (Kröner et al., 2001; Johnson et al., 2006; Fritz et al., 2013; Manda et al., 2019). Syn- and post-kinematic intrusions are also present in the Zomba Graben, as are dykes and minor intrusions that formed during at least two distinct Mesozoic phases of magmatism (Bloomfield, 1965; Eby et al., 1995). The Proterozoic Chingale Ring Complex and the Upper Jurassic-Lower Cretaceous Chilwa Alkaline Province, formed during a phase of NE-SW extension (orthogonal to the current extension direction; Bloomfield, 1965; Bloomfield and Garson 1965; Castaing, 1991; Eby et al., 1995), and the Zomba Massif and Chinduzi Hills plutons form local topographic highs (Fig. 4). Despite the anhydrous, cold continental crust setting, two hot springs have been studied to the northeast of the Zomba Graben, spatially associated with permeable fault systems and locally elevated heat flow (Fig. 3; Dulanya et al., 2010; Dávalos-Elizondo et al., 2021). Slickensides indicate that NNE-SSW striking faults in the Zomba Graben are almost pure dip-slip despite their obliquity to the regional ENE-WSW extension direction (Wedmore et al., 2020a), an observation that may be explained by deep-seated weaknesses that locally rotate fault strain (Williams et al., 2019).

This study examines three faults in the Zomba Graben: Mlunguzi and Chingale Step intrarift faults, and the Zomba border fault (Figs. 2 and 3). Currently, no chronostratigraphic data exists that can demonstrate whether these faults have been recently active. However, steep 5–40 m scarps (Fig. 4), triangular facets, offset alluvial fans, and footwall knickpoints imply that these faults have been active in the Late Quaternary (Wedmore et al., 2020a; Williams et al., 2022b).

Table 1

Fault type, sample lithology, fault geometry and strain distribution in the Zomba Graben. Data from this study and [Wedmore et al. \(2020a\)](https://doi.org/10.5281/zenodo.3582282).

Fault	Zomba	Chingale Step	Mlunguzi
Fault Type	Border	Intrarift	Intrarift
Footwall Lithology	Charnockite granulite	Norite	Hornblende-biotite-epidote gneiss
Length (km)	51	39	22
Strike (°)	025	022	013
Dip Direction	West	West	East
Fault Core Width (m)	Not observed	1–2	Not observed
Max. Fault Displacement (m)	620–870	165–235	75–105
Max. Segment Displacement (m)	620–870	140–195	N/A
Max. Displacement/Length Ratio	$1-1.5 \times 10^{-2}$	$4-6 \times 10^{-3}$	$3-5 \times 10^{-3}$
% of late-Quaternary strain (Wedmore et al., 2020a)	40 ± 17	42 ± 17	7 ± 1
Max. Scarp Height (m) (Wedmore et al., 2020a)	30.8 ± 13.7	35.3 ± 14.6	11.4 ± 1.4

3. Methods and materials

3.1. Constraining fault length and displacement in the Zomba Graben

We define fault length from the length of each of the three faults examined in this study using their surface scarp (Wedmore et al., 2020a; Williams et al., 2021), which is a minimum estimate as it does not include the subsurface extent of these faults (Kolawole et al., 2021);

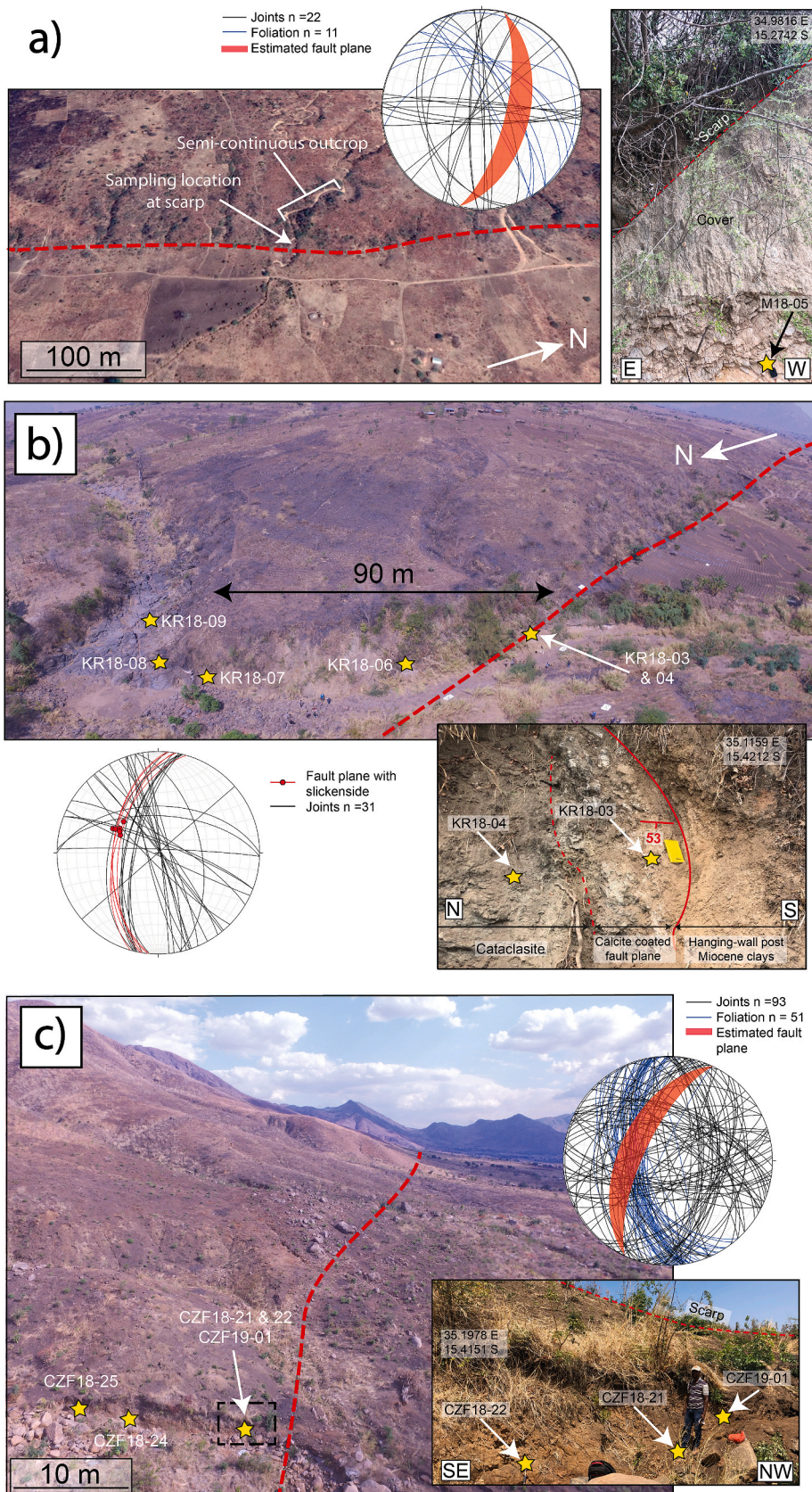


Fig. 5. Field and sampling localities for a) Mlunguzi transect, b) Chingale Step Kalira River transect, and c) Zomba fault Chingale Stream transect. For each fault panels show: footwall sampling localities in the context of the active fault trace (dashed red line), the exposure closest to the fault, and an equal area stereonet with fault, joint, and foliation orientations. Overview image in a) courtesy of Google Earth and shown with 3x vertical exaggeration. See Figs. S2–4 for further photos of sampling locations. (For interpretation of the references to colour in this figure legend, the reader is referred to the Web version of this article.)

Table 2

Samples and analyses carried out. 'Y' indicates samples used for respective analyses. Fault rocks are classified according to [Sibson \(1977\)](#).

Sample/ Fault	Distance from fault (m)	Lithology and field description	Elevation above fault trace (m)	Microfracture density quantification	SEM	XRD
<i>Mlunguzi</i>						
M18-06	0.0	Poorly foliated incohesive hornblende-biotite-epidote gneiss	–	–	Y	Y
M19-01	0.0	Poorly foliated incohesive hornblende-biotite-epidote gneiss	–	–	–	Y
M18-07	0.45	Poorly foliated incohesive hornblende-biotite-epidote gneiss	–	Y	–	Y
M18-05	1.9 ^a	Poorly foliated hornblende-biotite-epidote gneiss	–	Y	Y	Y
M18-03	26 ^b	Foliated hornblende-biotite-epidote gneiss	9	Y	Y	Y
M18-01	35 ^b	Foliated hornblende-biotite-epidote gneiss	9	Y	–	Y
M18-04	56 ^b	Foliated hornblende-biotite-epidote gneiss	7	Y	–	Y
M19-02	74.5 ^b	Foliated hornblende-biotite-epidote gneiss	7	Y	–	Y
<i>Chingale Step</i>						
KR18-03	0.00	Fault gouge	–	–	–	Y ^d
KR18-04	0.3 ^c	Cataclasite	–	–	Y	Y
KR18-05	0.6 ^c	Incohesive and altered norite	–	–	–	Y
KR18-06	4.3	Incohesive and altered norite	–	Y	Y	Y
KR18-07	9.0	Incohesive and altered norite	–	Y	–	Y
KR18-08	9.5	Norite	–	Y	–	Y
KR18-09	18 ^b	Norite	4	Y	Y	Y ^d
<i>Zomba</i>						
CZF19-01a	0.0 ^a	Incohesive charnockite	–	–	Y	Y
CZF18-21	0.55 ^a	Incohesive charnockite	–	Y	–	Y
CZF18-22	2.6 ^a	Incohesive charnockite	–	Y	–	Y
CZF18-23	5.2 ^a	Incohesive charnockite	–	Y	Y	Y
CZF18-24	10.4 ^a	Incohesive charnockite	–	Y	–	Y
CZF18-25	15.5 ^b	Incohesive charnockite	5.5	Y	–	Y
CZF18-26	59 ^b	Charnockite	20.5	Y	–	Y
CZF18-27	109.5 ^b	Charnockite	17.5	Y	Y	Y

^a Horizontal distance from fault recorded by tape measure, then corrected for fault dip.

^b Horizontal distance from fault calculated from GPS coordinates, then corrected for elevation difference between sample and fault, and fault dip.

^c Distance from fault measured along line oblique to fault by tape measure, adjusted to horizontal distance from fault then corrected for fault dip.

^d Analysed previously by [Williams et al. \(2019\)](#).

[Williams et al., 2022b](#)). To constrain maximum fault displacement (D_{\max}), we first obtain an estimate of fault throw from combining the footwall relief ([Fig. 4](#)) and thickness of syn-rift sediments measured from nearby boreholes ([Fig. 3](#); [Bloomfield, 1965](#); [Bloomfield and Garson, 1965](#)). Assuming pure dip-slip ([Williams et al., 2019](#)), we then project this fault throw estimate into fault dip to obtain the fault's displacement.

For the single-segment Mlunguzi fault we estimate throw using the maximum footwall relief and syn-rift sediment thickness. Hence, our displacement estimate is indicative of D_{\max} . Similarly, for the multi-segment Chingale Step and Zomba faults we consider these fault's D_{\max} when discussing their D_{\max} -length scaling, for consistency with other compilations (e.g. [Lathrop et al., 2022](#)). However, for fault zone width-displacement scaling, we consider the maximum displacement along the fault segment that was sampled (Chingale Step South and Zomba fault Chingale Stream segments; [Fig. 4](#); [Table 1](#); [Wedmore et al., 2020a](#); [Williams et al., 2021](#)). This displacement measurement is therefore representative of the fault segment in which the fault zone width was measured.

3.2. Field observations and sampling

We collected structural measurements and outcrop descriptions along transects where ephemeral streams have incised into and provide semi-continuous outcrop sequences through the footwall of the three faults (Mlunguzi fault, one transect; Chingale Step fault, two transects; Zomba fault, two transects; [Fig. 5](#)). Each transect was made within a relatively straight fault segment ([Fig. 3](#)) so that along-strike geometrical complexities such as bends or jogs do not influence our fault width estimates ([Kim et al., 2004](#)).

In addition, a total of 23 samples were collected along three of the transects (one transect per fault) for microstructural and compositional analyses (8 from the Mlunguzi fault, 7 from the Kalira River through the

Chingale Step fault, and 8 from the Chingale Stream through the Zomba fault; [Fig. 5](#), [Table 2](#). Samples were selected so that they spanned the range of units recognised in our outcrop descriptions: intact background protolith, incohesive protolith where the original rock fabrics are preserved, and fault gouges and cataclasite. [Table 2](#) lists brief sample descriptions, the distance of each sample from the fault scarp, as calculated below, and the microstructural and compositional analyses performed during this study. Foliated samples are cut perpendicular to foliation, whereas non-foliated samples are randomly oriented. The lack of a defined preferred microfracture orientation in these samples (see [Section 6](#)) means that randomising their orientation does not bias our microfracture density analysis. More details on sample preparation are given in the Supplementary Information.

Sampling locations along our transects were either recorded using handheld GPS (accurate to ~ 3 m) or measured directly as fault-normal distance in the field by tape measure. The distance of each sample from the fault scarp is reported orthogonal to fault plane ([Fig. S1](#)). For samples > 12.5 m from the scarp, we correct for the elevation difference between the samples and the fault trace using a TanDEM-X digital elevation model with an absolute vertical mean error of ± 0.2 m, and a horizontal resolution of 12.5 m ([Wessel et al., 2018](#)). For samples closer to the fault scarp, we assume that samples are at the same elevation as the fault trace.

3.3. Microfracture density analysis

Systematically measuring spatial variations in microfracture density around faults can constrain fault damage zone width ([Anders and Wiltshcko, 1994](#); [Wilson et al., 2003](#); [Mitchell and Faulkner, 2009](#); [Wedmore et al., 2020b](#)). In this study we measured the microfracture density of areas within suitable samples, selected through petrographic analysis to include those with a > 50 % proportion of quartz or feldspar



Fig. 6. Photos of field exposures or hand sample collected from each transect. a-c) Distance of sampling point or sample from a) Mlunguzi fault, b) Chingale Step fault at Kalira River transect and c) Zomba border fault at Chingale Stream. Exposures range from incohesive rock (left) to intact background protolith (right). White box indicates sampling point. d-e) Additional field transects showing incohesive exposure (left), and intact background protolith (right) for d) Chingale Step fault at Lintipe River and e) Zomba fault at Namitembo. See [Figs. S2-5](#) for further photos of fault transects.

grains but exclude those closest to the fault which contain such extensive damage that microfractures cannot be recorded accurately (Table 2). To measure microfracture density, we use a method previously applied by Wedmore et al. (2020b) to study the damage zone of the Thyolo fault in southern Malawi. In this approach, square photomicrographs were taken from three areas within each analysed thin section at 2.5x magnification in both plane polarised light (PPL) and cross-polarised light (XPL). Microfractures in quartzofeldspathic grains were then traced in Adobe Illustrator, using a maximum zoom of 400 %, and the total length of microfractures present was calculated using FracPaQ 2.6.1.0 (Healy et al., 2017). The total quartzofeldspathic domain area in each image was then calculated by masking all non-quartzofeldspathic grains in ImageJ. The microfracture density for individual areas can then be expressed using the equation:

$$\text{Microfracture density} \left(\frac{1}{\text{mm}} \right) = \frac{\text{Total microfracture length (mm)}}{\text{Sampling Area (mm}^2\text{)}} \quad (1)$$

The reported microfracture density (mm^{-1}) for each sample is the area-weighted mean value of the three areas, with the range of values between the areas representing our uncertainty. Further details of this analysis are given in the supplementary information.

3.4. X-Ray Diffraction

X-Ray Diffraction (XRD) analysis was used to constrain bulk rock mineralogy, identify fault zone alteration, and to test whether microfracture density variations between samples are related to lithological variations. XRD patterns were obtained using a Philips PW1710 Automated Powder Diffractometer with X-Rays generated using $\text{CuK}\alpha$ radiation at 35 kV and 40 mA at the Cardiff University X-Ray Diffraction Facility, and were run over the range of 2° – 70° in steps of 0.020° 2θ . Analysis was then performed using the computer software PW1877 APD version 3.6 and the identification software PW1876 PC-Identify version 1.0 b. Phase proportions were calculated semi-quantitatively from the area of the primary peak for each mineral phase and normalised to 100 %, and so do not include estimates of amorphous or unidentified material. Further details on sample preparation for XRD analysis are included in the supplementary information.

3.5. Scanning Electron Microscopy

Three samples were selected from each transect for Scanning Electron Microscopy (SEM) analysis (Table 2). Each sample was coated with 10 nm of carbon prior to analysis, performed on a Zeiss Sigma HD FEG Analytical Scanning Electron Microscope (ASEM) in the Cardiff University Electron Microbeam facility. The ASEM operated with a beam energy of 15 keV, a 60 μm aperture and at a working distance of 8.9 mm with high current and high vacuum conditions.

4. Zomba Graben fault displacements

Boreholes indicate that the thin syn-rift sediment cover in the Zomba Graben is ~ 30 – 50 m thick (Fig. 3; Habgood, 1963; Bloomfield, 1965). This comparatively thin syn-rift sediment sequence, coupled with the maximum fault and fault segment escarpment heights (28–520 m; Fig. 4) indicates the studied faults have accumulated throws of ~ 68 – 560 m. The Chingale Step fault plane dips at 53° at the Kalira River transect, however no such measurement was possible for the Mlunguzi and Zomba faults. Therefore, we estimate maximum fault and fault segment displacement using a dip range of 40 – 65° , which is consistent with the range of fault dips observed elsewhere in Malawi (Mortimer et al., 2007; Kolawole et al., 2018; Williams et al., 2019; Stevens et al., 2021) and within the range of normal fault dips resolved from earthquake focal mechanisms (Collettini and Sibson, 2001). We estimate D_{max} of 75–105 m, 165–235 m and 620–870 m for Mlunguzi, Chingale Step and Zomba

faults, respectively, giving respective D_{max} -length ratios of 3 – 5×10^{-3} , 4 – 6×10^{-3} , and 1 – 1.5×10^{-2} . The displacement estimate for the Chingale Stream segment of the Zomba fault, within which we performed our field and sampling transects, is the same as the D_{max} . However, along the Chingale Step fault South segment, across which the Kalira River transect is located, maximum displacement is estimated to be 140–195 m (Table 1).

There is uncertainty in our syn-rift sediment thickness estimates as not all have nearby boreholes that penetrated basement (Fig. 3). However, a thin (< 150 m) syn-rift sediment package in the Zomba Graben is consistent with observations from sites at the southern end of the graben where basement is exposed in the hanging wall of the Zomba Graben faults (Fig. 2), and with other estimates of syn-rift sediment thicknesses in southern Malawi using geophysical surveys (Ojo et al., 2022a). Furthermore, fault scaling data is typically plotted in log-log space (e.g., Torabi and Berg, 2011; Lathrop et al., 2022), and for our fault displacement estimates to significantly misrepresent where the Zomba Graben faults plot in this space would require that these faults had multi-km displacements instead; an inference which we consider extremely unlikely given the available data.

5. Fault zone field descriptions

The footwall of the 22 km long Mlunguzi fault is exposed along an unnamed stream adjacent to the scarp (Fig. 5a). Here there is a ~ 2 m wide exposure of weakly foliated incohesive jointed amphibolite facies hornblende-biotite-epidote gneiss (Figs. 5a and 6a; Bloomfield and Garson, 1965). Immediately below the Mlunguzi fault scarp, we excavated the topsoil to expose and sample a fine-grained white unit. Two samples were also taken 0.45 m and 1.9 m from the fault, where the original gneissic fabric is preserved, but the rock mass is incohesive and contains abundant joints (Fig. 6a). There is no exposure along the unnamed stream between 2 and 26 m from the scarp, but a semi-continuous exposure comprising hornblende-biotite-epidote gneisses with concordant pegmatites is observed further up the stream (Figs. 5a and 6a). Locally, the gneissic foliation is folded, and there are steeply-dipping N–S and E–W striking joint sets. However, from the intact nature of this exposure (Fig. 6a), we infer that this exposure, > 26 m from the scarp, represents the background protolith. At this transect, the \sim N–S striking Mlunguzi fault cross-cuts the moderately dipping NW–SE striking foliation (mean and 1 standard deviation strike and dip: $135 \pm 23^\circ$ and $58 \pm 21^\circ$ respectively; Fig. 5a).

The Kalira River exposes a footwall section of the 39 km long Chingale Step fault scarp where it juxtaposes post-Miocene hanging-wall alluvium against footwall syn-to-late kinematic Proterozoic norite (Fig. 5b, S3a; Bloomfield, 1965). Here, the fault plane itself is exposed and is coated by a calcareous gouge that exhibits near dip-slip slickensides (Figs. S3a and b; Williams et al., 2019; Wedmore et al., 2020a). Adjacent to the scarp is a 1–2 m thick calcite-rich cataclastic fault core (Fig. 5b) and a 9 m thick incohesive norite unit that contains E–W striking, steeply dipping, Cretaceous Chilwa Alkaline Province dykes (Figs. S3c and d; Bloomfield, 1965). Samples were taken from the incohesive norite unit, at respective distances of 4.30 m and 9.02 m from the fault (Fig. 6b). Exposure immediately beyond this unit, including samples taken 9.50 m and 18 m from the fault (Fig. 6b), comprises unaltered and intact norite with regular N–S and E–W striking steeply dipping joint sets. This unit is interpreted to represent the background protolith, and is exposed up to at least 100 m from the scarp (Figs. S3e and f).

Another exposure through the Chingale Step fault's footwall is observed where it crosses the Lintipe River, 9 km north of the Kalira River. The faulted contact is not exposed here, but a thin unit (17 m horizontal thickness, 10 m thickness when measured orthogonal to the projected fault plane) of poorly foliated incohesive biotite gneiss is observed in the river bank and on the river bed (Fig. 6d and S5). Immediately beyond the exposed incohesive unit the biotite gneiss is more intact with a prominent steep W-dipping foliation (Fig. 6d and S5).

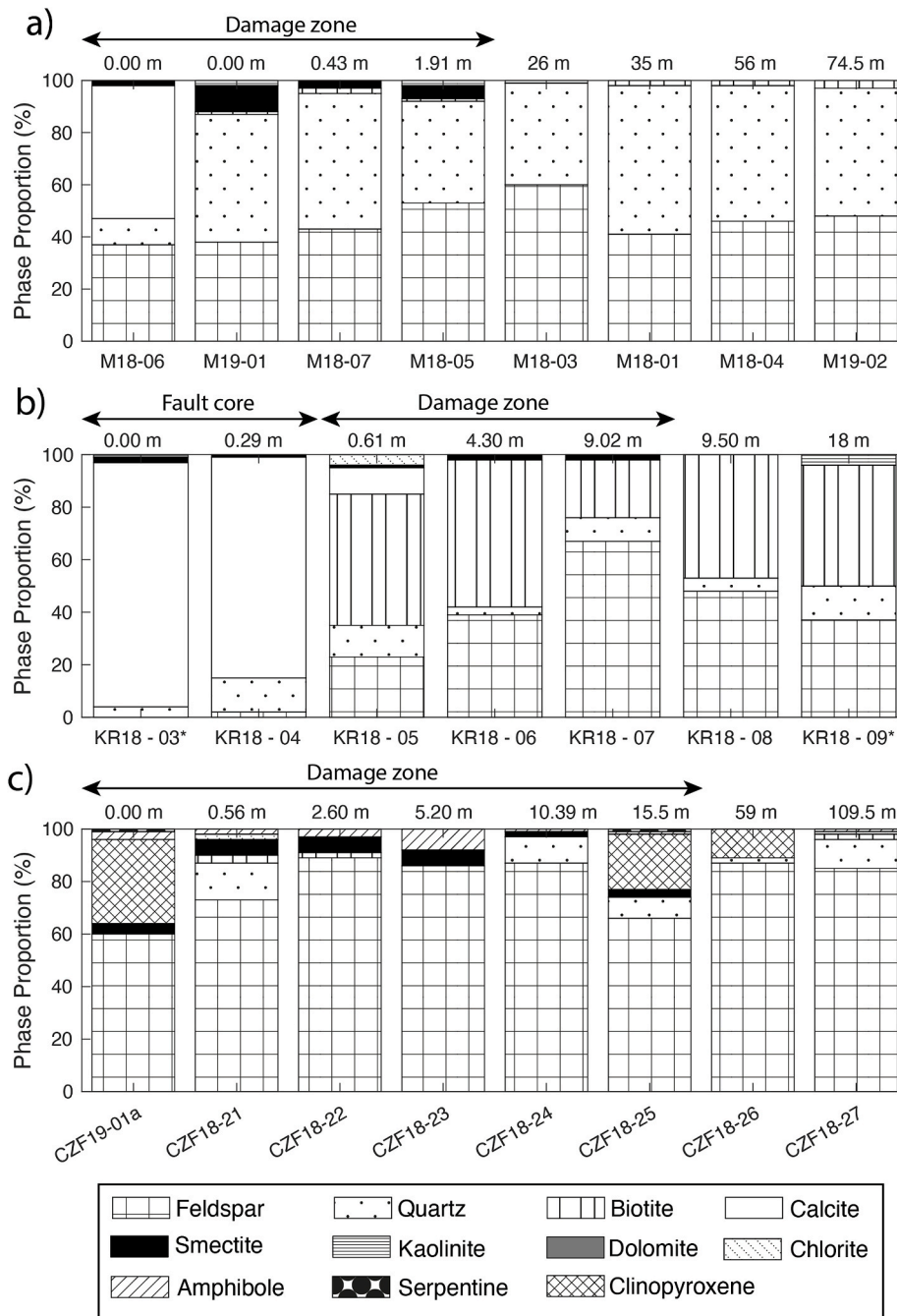


Fig. 7. Mineralogy results for a) Mlunguzi, b) Chingale Step and c) Zomba fault transects from XRD analysis. The greatest change in mineralogy occurs closest to Mlunguzi and Chingale Step faults where calcite dominates sample composition. 1–10% smectite is detected within each fault zone, but no other significant trend is present. Results are semi-quantitative and normalised, and therefore do not contain estimates of unidentified or amorphous material. *Analysis of samples KR18-03 and KR18-09 was undertaken by Williams et al. (2019). See Table S1 for data.

that is locally folded and cut by discordant pegmatites.

The 51 km long Zomba fault is exposed along the Chingale Stream (Fig. 5c) which incises a 20 m wide sequence of incohesive poorly-foliated charnockite granulite adjacent to the base of the fault's Late Quaternary scarp (Fig. 5c and S4a,c; Bloomfield, 1965). Within this sequence, cm-thick pegmatite veins are separated by up to 30 cm along small faults (Fig. S4d); however, we find no other evidence of shear displacements or fault rocks at this locality. Six samples taken 0–15.5 m from the fault scarp are all intensely fractured, and increasingly friable with proximity to the fault (Fig. 6c). At distances ≥ 59 m from the scarp, the charnockite gneisses are cohesive, well foliated, and locally contain pods of plagioclase granulites and feldspathic bands (Figs. S4f and e; Bloomfield, 1965). Samples collected 59 m and 109.5 m from the fault (Fig. 6c) are thought to represent the background protolith. At this transect, the 035° striking Zomba fault is oblique to the moderately (62

$\pm 10^\circ$) west-dipping, N–S striking ($169 \pm 13^\circ$) foliation (Fig. 5c). However, at the regional (10–100 km) scale, the Zomba fault is broadly parallel to regional WNW-dipping metamorphic fabrics (Williams et al., 2019).

Weakly-foliated Proterozoic syenites are also mapped in the hanging wall of the Zomba fault near this transect (Bloomfield, 1965); however, the closest exposure (140 m from the fault plane) shows no evidence for fracturing, alteration, or any other indication for deformation along the Zomba fault. At Namitembo, ~ 10 km to the north, a 5 m wide unit of incohesive foliated charnockite gneisses with a moderately NW dipping foliation is exposed immediately below a Zomba fault scarp (Fig. 6e). The maximum thickness of this unit, measured orthogonal to the fault plane and as constrained by the presence of intact well foliated gneiss in the next exposure (Fig. 6e), is 38 m. No fault contact or fault rocks were observed at this locality.

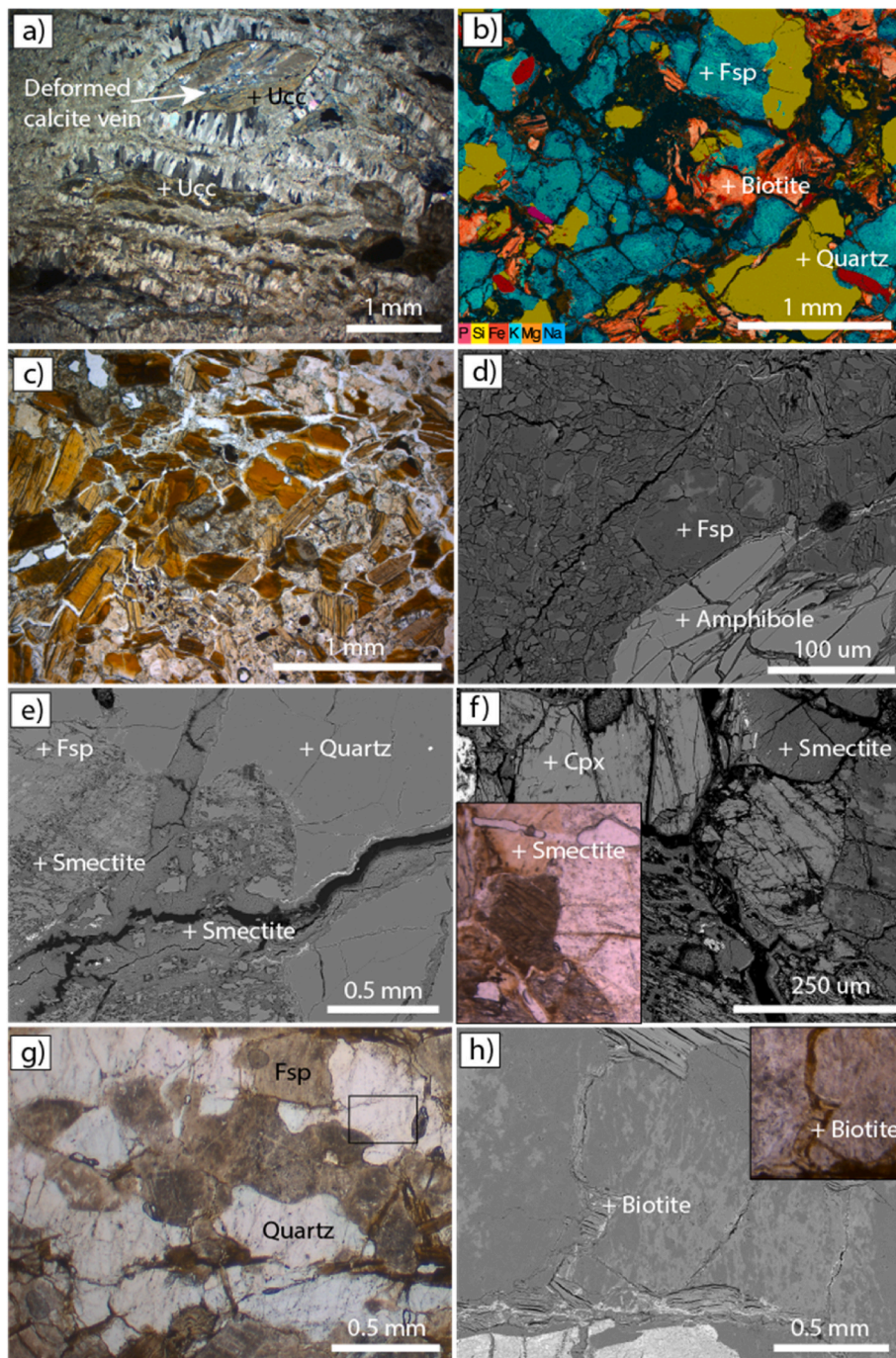


Fig. 8. Fault zone microstructures and chemical alteration. a) Photomicrograph in crossed-polarised light of Chingale Step fault core, showing multiple phases of ultracataclasite (Ucc) development and calcite veining. b) Backscatter image and element map overlay of fractured Mlunguzi sample taken from the fault scarp, showing <1 mm fragments with no evidence of shearing. c) Photomicrograph of Chingale Step sample taken 0.6 m from fault, fractured into <0.5 mm fragments with no evidence of shearing. d) Backscatter image of sample taken 5.2 m from Zomba fault, highly comminuted into 5–100 μm fragments which show little to no displacement. e) Backscatter image showing smectite growth in fractures and feldspar grain margins. f) Backscatter image of Zomba sample taken <1 m from fault, showing smectite fracture fill and discoloured amphibole grains entirely altered to smectite in photomicrograph inset. g) Photomicrograph of Mlunguzi sample taken 26 m from fault, showing extensive chemical alteration of feldspar which obscures fractures, and black box highlights fluid inclusion planes in quartz. h) Backscatter image of Mlunguzi sample taken 26 m from fault showing biotite growth in fractures, which is observed in this sample only. Fsp = Feldspar, Cpx = clinopyroxene.

At all fault exposures, local joint orientations are parallel to regional, moderately to steeply dipping, N–S and E–W striking joint sets (Williams et al., 2019), except at the Kalira River Chingale Step fault exposure, where there is an additional NW–SE steeply dipping joint set (Fig. 5).

6. Microstructure and fault zone alteration

6.1. Fault core

Within the 1–2 m wide calcite-rich (> 80 wt %; Fig. 7) Chingale Step fault core both deformed and undeformed calcite veins are present at the microscale, surrounding and within clasts of norite-derived ultracataclasite (Fig. 8a), whilst calcite-rich fault gouge contains clasts of mesocataclasite. In the undeformed calcite veins, elongate, blocky

grains are observed with long axes approximately orthogonal to fracture margins (Fig. 8a). Calcite is absent, or only detected in minor amounts, in all other Chingale Step fault samples (Fig. 7). No fault cores were observed along the Zomba or Mlunguzi faults, however this could be due to erosive processes or incomplete exposure (Figs. S2 and S4).

6.2. Wall rock fracturing and mineralisation

Samples taken adjacent to the Mlunguzi fault scarp, up to 0.6 m from the Chingale Step fault scarp, and up to 5.2 m from the Zomba fault scarp are highly fragmented but lack signs of shearing, with grain boundaries and fragments aligned across fractures (Fig. 8b,c,d). At these distances, Mlunguzi and Chingale Step samples are fragmented into ≤ 1 mm and ≤ 0.5 mm clasts, respectively (Fig. 8b and c), while 5.2 m from the Zomba

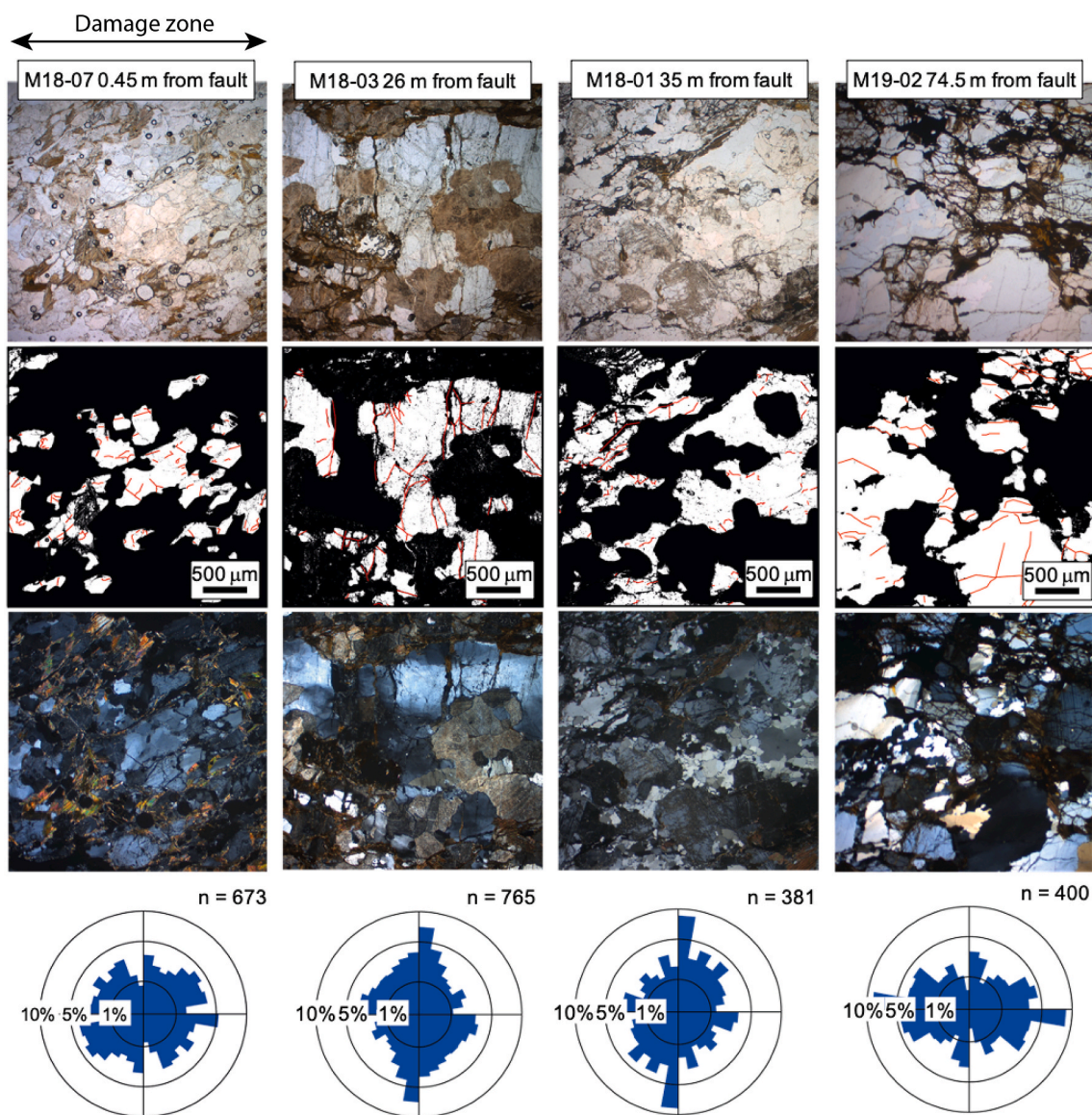


Fig. 9. Traced sample area examples from Mlunguzi fault transect, showing from top to bottom: sample area photomicrographs, traced fractures in red with excluded areas blanked out, sample area photomicrographs in cross-polarised light, and rose graphs showing the orientation of all traced fractures for each sample (combined from three traced areas per sample). Fractures are not traced in feldspar domains due to extensive alteration of feldspar to clay, which obscures fractures in key samples such as M18-03 26 m from fault. See Fig. S6 for all examples from this transect. (For interpretation of the references to colour in this figure legend, the reader is referred to the Web version of this article.)

fault grains are shattered into intragranular fragments with sizes between 5 and 100 μm (Fig. 8d).

Calcite comprises $\sim 10\%$ of the wall rock sample closest to Chingale Step fault core, and $> 50\%$ of one of the samples taken adjacent to Mlunguzi fault scarp (Fig. 7). Within 2 m, 4 m and 16 m of Mlunguzi, Chingale Step and Zomba faults, respectively, numerous open or smectite-filled, 45–70 μm wide fractures are observed, commonly truncating more frequent closed fractures (Fig. 8e). Smectite is detectable by XRD in these samples, present in weight proportions of 2–10 % (Mlunguzi fault), 1–2 % (Chingale Step fault) and 2–6 % (Zomba fault; Fig. 7). Smectite occurs as either single or multiple growth phases within open fractures, within margins of fractured grains (Fig. 8e), or as the alteration product of amphibole (Fig. 8f). Alteration products such as kaolinite, chlorite and serpentinite are detected in minor amounts (1–4 wt %) in some samples, however, unlike calcite and smectite, their presence shows no correlation with distance from fault (Fig. 7).

At distances ≥ 9.5 m from the intrarift faults, and ≥ 59 m from the Zomba border fault, fractures are typically infrequent and < 5 μm thick.

A deviation from this general observation occurs 26 m from the Mlunguzi fault, where wide fractures (~ 60 μm width) are predominantly biotite- or iron oxide mineralised (Fig. 8g and h). This sample is anomalous compared to the rest of the transect, with discolouration of feldspar grains, and undulose extinction and fluid inclusion planes in quartz grains, present to a far greater degree than elsewhere along the transect (Fig. 9).

6.3. Microfracture density results

Along the Mlunguzi fault transect, microfracture densities are between 0.75 and 1.0 mm^{-1} in samples ≤ 26 m from the fault, and decrease to 0.25–0.45 mm^{-1} in samples 35–75 m from the fault (Fig. 9). The range in microfracture density within the transect is 0.75 mm^{-1} , which is the smallest range of the three fault transects.

Microfracture densities along Chingale Step fault transect show a gradual decrease with increasing distance from the fault, from 2.9 mm^{-1} to 0.75 mm^{-1} , with a range of 2.0 mm^{-1} (Fig. 10). Here, in regions

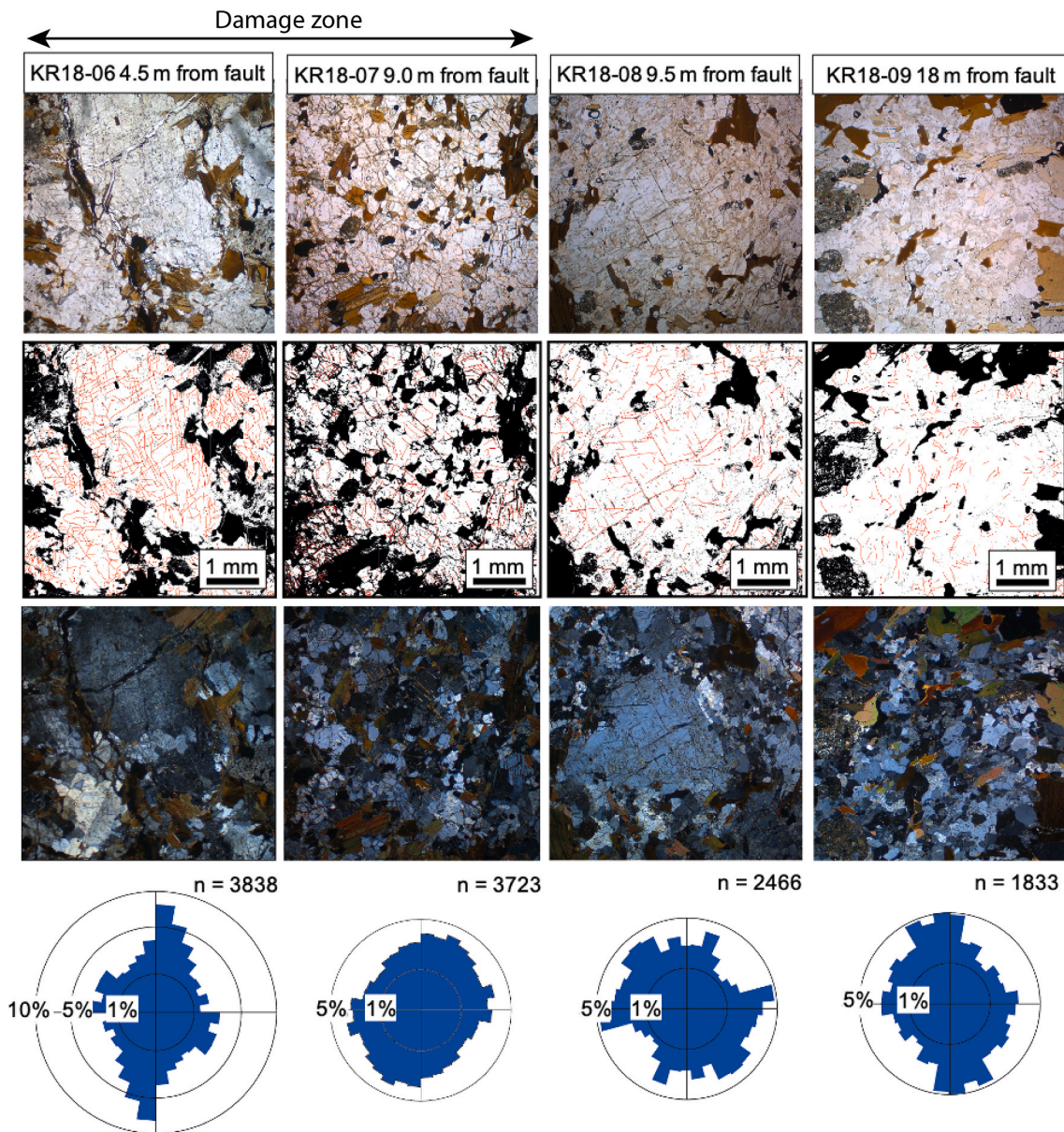


Fig. 10. Traced sample area examples from Chingale Step fault transect, showing from top to bottom: sample area photomicrographs, traced fractures in red with excluded areas blanked out, sample area photomicrographs in cross-polarised light, and rose graphs showing the orientation of all traced fractures for each sample (combined from three traced areas per sample). Feldspar dominates quartzofeldspathic domains across this transect, and at this scale fractures appear to exploit feldspar cleavage to a greater extent in larger 3–4 mm grains (KR18-06 and KR18-08), than in smaller <0.5 mm grains (KR18-07 and KR18-09). (For interpretation of the references to colour in this figure legend, the reader is referred to the Web version of this article.)

dominated by large feldspar grains, mineralogy and grain size variability appears to influence microfracture density across these samples. For example, in coarser-grained samples, 4.5 m and 9.5 m from the fault, microfractures exploit cleavage planes in larger 3 mm feldspar grains to a greater extent than in smaller < 0.5 mm grains in samples 9 m and 18 m from the fault (Fig. 10). Along the Zomba fault transect, microfracture densities generally decrease from 4.1 mm^{-1} , < 1 m from the fault scarp, to 0.3 mm^{-1} , 110 m from the fault, giving the greatest range in microfracture densities across the three transects of 3.8 mm^{-1} (Fig. 11).

7. Determining damage zone and fault zone widths in the Zomba Graben

7.1. Microstructural constraints

Damage zone width is typically defined by the fault-normal distance

where fracture density is elevated above a threshold background value (e.g. Mitchell and Faulkner 2009; Savage and Brodsky, 2011). We therefore first use our microfracture density observations to constrain the footwall damage zone width of faults in the Zomba Graben. Given the sparse nature of the sampling, this analysis can only constrain damage zone width to within the distance range between the sample farthest from the fault but inside the inferred damage zone, and the sample closest to the fault which lies within background microfracture densities.

For the Mlungusi fault, the spatial variation in microfracture density alone suggests a 26–35 m wide footwall damage zone (Fig. 12a). For the Chingale Step transect, the microfracture density decreases at all distances from the fault, which could mean that the samples do not extend across the full width of its footwall damage zone. However, as explained in Section 6.3, grain size and mineralogy variability influences microfracture density in these samples, and so the sample 9.5 m from the fault

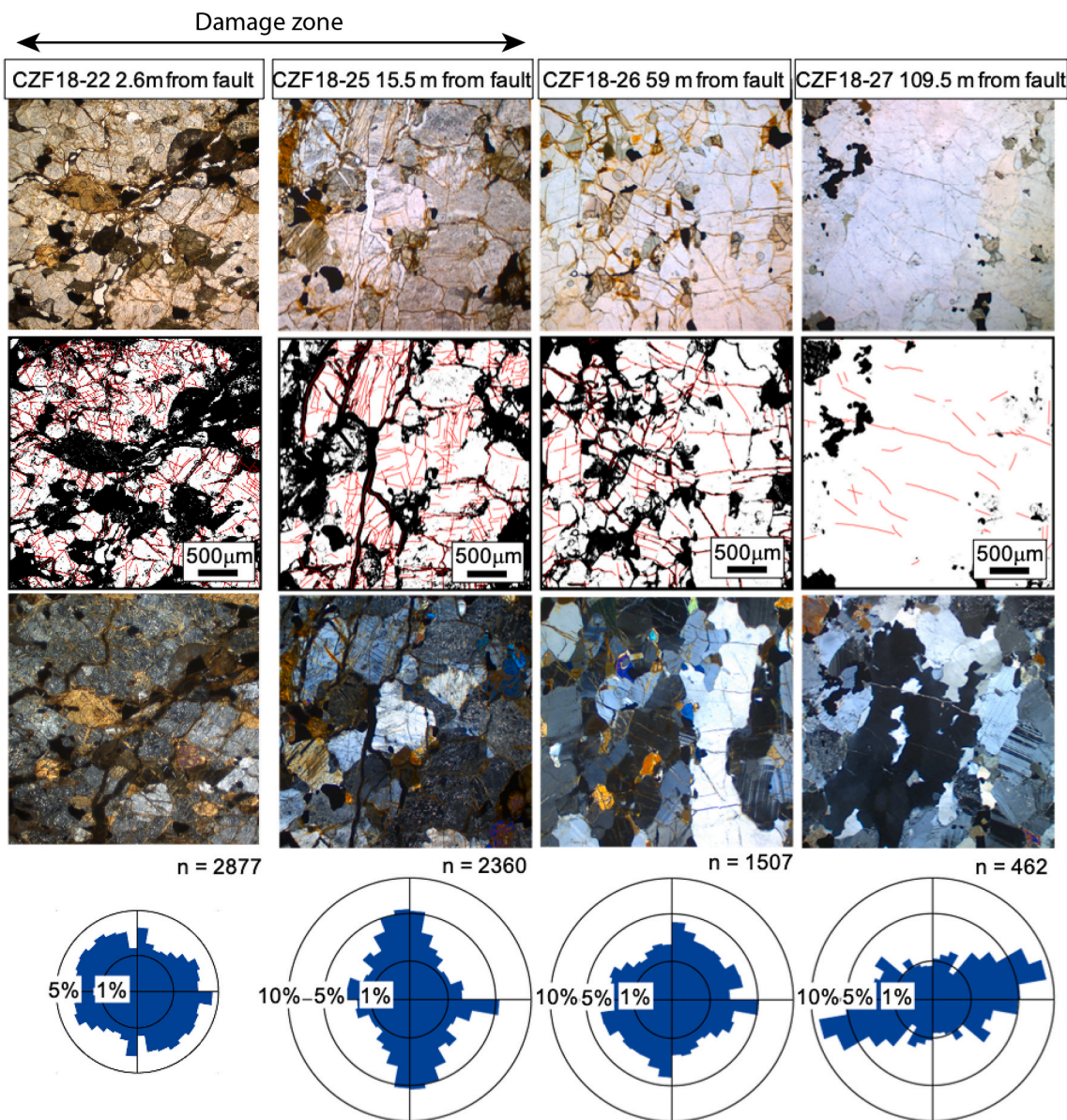


Fig. 11. Traced sample area examples from Zomba fault transect, showing from top to bottom: sample area photomicrographs, traced fractures in red with excluded areas blanked out, sample area photomicrographs in cross-polarised light, and rose graphs showing the orientation of all traced fractures for each sample (combined from three traced areas per sample). Within 15.5 m of the fault many grains are chemically altered to clay, and contain frequent, open intergranular fractures and extensive intragranular fractures. In the two samples furthest from the fault grains are not chemically altered and contain less frequent, closed fractures. See Fig. S7 for all examples from this transect. (For interpretation of the references to colour in this figure legend, the reader is referred to the Web version of this article.)

may have a disproportionately high microfracture density. If true, the footwall damage zone may be defined by the interval 9–9.5 m from the fault, across which a sharp decrease in microfracture density from $> 2 \text{ mm}^{-1}$ to $< 1.4 \text{ mm}^{-1}$ occurs.

For the Zomba Fault, the distinct interval of samples with microfracture densities $4.1\text{--}2.5 \text{ mm}^{-1}$ indicate that the damage zone is $> 15 \text{ m}$ wide. The sample at 59 m has a higher microfracture density than the sample 110 m from the fault, so it is unclear from these data alone whether these samples represent damage zone fracturing or random variations within the microfracture density of the protolith. In summary, using microfracture density alone to constrain the footwall damage zone width of the Zomba Graben faults provides poorly constrained width estimates. Furthermore, the samples we collected have experienced deformation and igneous intrusion prior to current rifting (Section 2) and it is possible that they contain microfractures from these events. Therefore, below we also consider our compositional analyses and field

observations when estimating damage zone width, as these observations can help determine whether the microfractures are a result of upper-crustal deformation.

7.2. Extent of chemical alteration zone

Our XRD analyses indicate the presence of 2–10% smectite is limited to, and ubiquitous across, samples within 2 m of the Mlunguzi fault, 9 m of the Chingale Step fault, and 15.5 m of the Zomba fault (Figs. 7 and 12). The localised presence of smectite in samples closest to the faults is also consistent with observations from our SEM analysis that it occurs as a fracture fill and through the replacement of grains such as amphibole (Fig. 8). Smectite is a low ($< 120 \text{ }^\circ\text{C}$) temperature clay and so its presence in samples closest to the faults may reflect upper-crustal damage zone fracturing and subsequent mineralisation. It is also notable that the aperture of microfractures is wider in samples that contain smectite

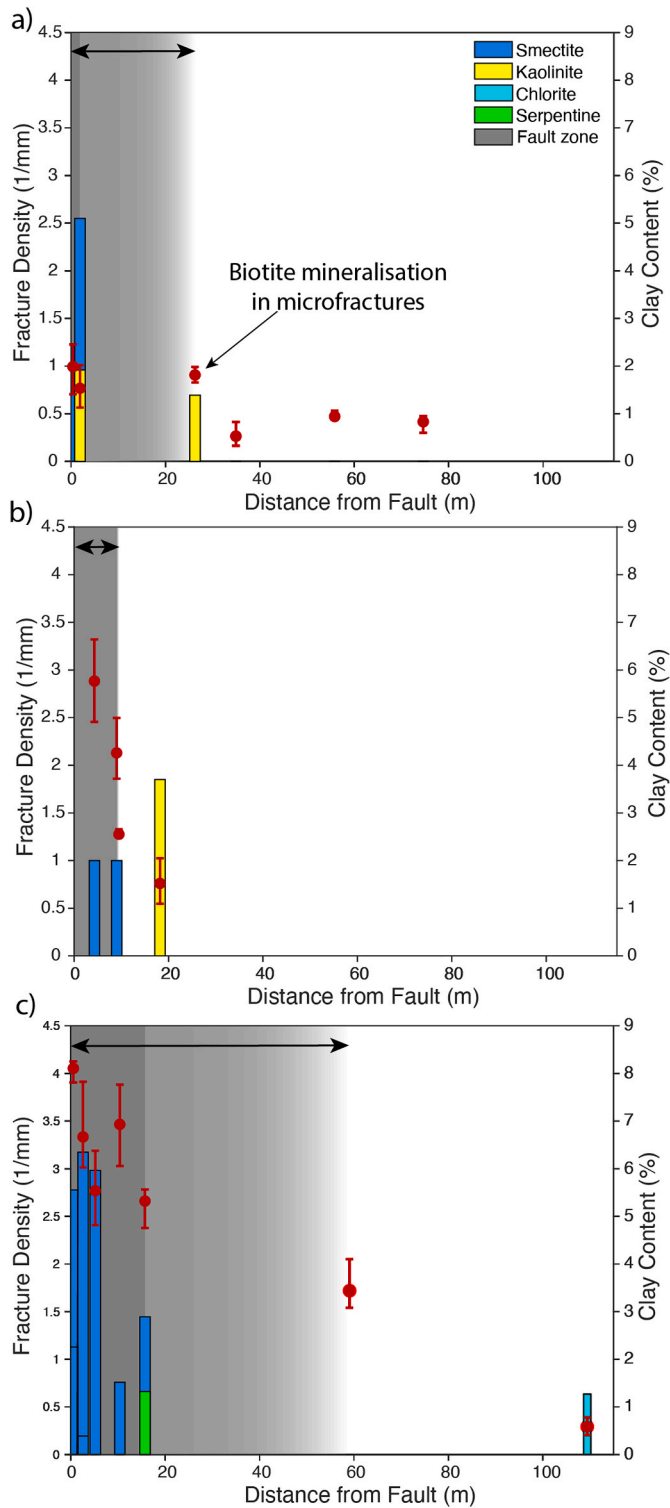


Fig. 12. a-c) Microfracture densities combined with field and petrological observations, and XRD results to give estimated footwall fault zone widths for a) Mlunguzi intrarift b) Chingale Step intrarift and c) Zomba border fault. Solid grey shading spans fault zone data points, whereas gradational grey shading indicates the distance between the furthest damage zone data point and closest background data point constrain the upper and lower estimated fault zone widths. The black double-headed arrow indicates fault zone widths as estimated in the field. Smectite is present in all fault zone samples. Anomalous data point 26 m from fault in a) contains localised alteration and deformation outlined in Section 7.2 See Table S2 for data.

(45–70 μm vs < 5 μm wide; Section 6.2).

For the Chingale Step fault, the extent of smectite supports the inference that its footwall damage zone is 9–9.5 m wide, whilst for the Zomba fault, its absence in samples 59 and 109.5 m from the fault indicates its footwall damage zone is 15.5–59 m wide. For the Mlunguzi fault, the absence of smectite in the sample 26 m from the fault is inconsistent with the elevated microfracturing in this sample (Fig. 12a). Instead, biotite and Fe-oxide microfracture mineralisation and fluid inclusion planes are the dominant microstructures. Since fluid inclusion planes and biotite mineralisation are generally associated with temperatures > 300 °C (Jacobs and Parry, 1976), and Fe is comparatively rare in crustal fluids in Malawi (Dávalos-Elizondo et al., 2021), we infer that these microstructures represent an earlier high temperature deformation event prior to the recent exhumation of the rocks. If true, this sample is not representative of Mlunguzi fault damage zone microfracturing, and suggests that its footwall damage zone width is actually 2–26 m.

7.3. Field constraints

We did not attempt to quantify macroscale fracture density along our field transects, as it is difficult to preserve macroscale fractures in the relatively soft and incohesive exposure closest to the faults. Instead, we infer the incohesive nature of the rock mass in these exposures is itself a result of fault zone microfracturing and compositional changes, and hence it can be used a proxy for damage zone width. Using this constraint, we estimate that the footwall damage zone is 2–26 m wide for the Mlunguzi fault, 9–9.5 m wide at Kalira River and 10 m wide at Lintipe River for the Chingale Step fault, and 15.5–59 m wide at Chingale Stream and 5–38 m wide at Namitembo for the Zomba fault (Figs. 3 and 6). We consider the variation in damage zone width between the two Chingale Step transects to be within error, given the natural variability between the transect lithologies. Overall, our field observations therefore support the estimates from the microfracture density and compositional analysis that the footwall damage zone of Mlunguzi, Chingale Step, and Zomba faults are 2–26 m, 9–10 m, 16–59 m wide respectively.

7.4. Fault zone widths

Strictly speaking, the term fault zone width considers the combined width of the fault core and damage zone. For the Zomba Graben faults in this study, we have only been able to measure footwall damage zone width, and hence some allowance must be made for the unknown width of the hanging-wall damage zone and, for the Zomba and Mlunguzi faults, the width of the fault core. For the first point, we note that the asymmetric stress field around non-vertical faults means normal fault hanging-wall and footwall damage zones can have different widths (Berg and Skar, 2005; Ota et al., 2005; Ma, 2009; Boncio et al., 2012). However, to compare our results with global displacement-width datasets of different fault types (normal, thrust and strike-slip faults; Savage and Brodsky, 2011; Torabi et al., 2020), we double the footwall fault zone width to obtain estimates for the total fault damage zone width (following Savage and Brodsky, 2011). Fault cores are typically much thinner than damage zones (Torabi and Berg, 2011), and so we assume that uncertainty in the thickness of the Mlunguzi and Zomba fault cores is contained within the uncertainty of their damage zone width. Given these assumptions, our footwall damage zone widths of 2–26 m (Mlunguzi intrarift fault), 9–10 m (Chingale Step intrarift fault) and 16–59 m (Zomba border fault), give total fault zone widths of 4–52 m, 18–20 m and 32–118 m, respectively.

We note here that if the footwall outcrops from which the field and microstructural data were collected from were exposed early during fault growth, then they would not have recorded wall rock deformation during subsequent displacement along the Zomba Graben faults and these fault zone widths would be underestimates. However, the

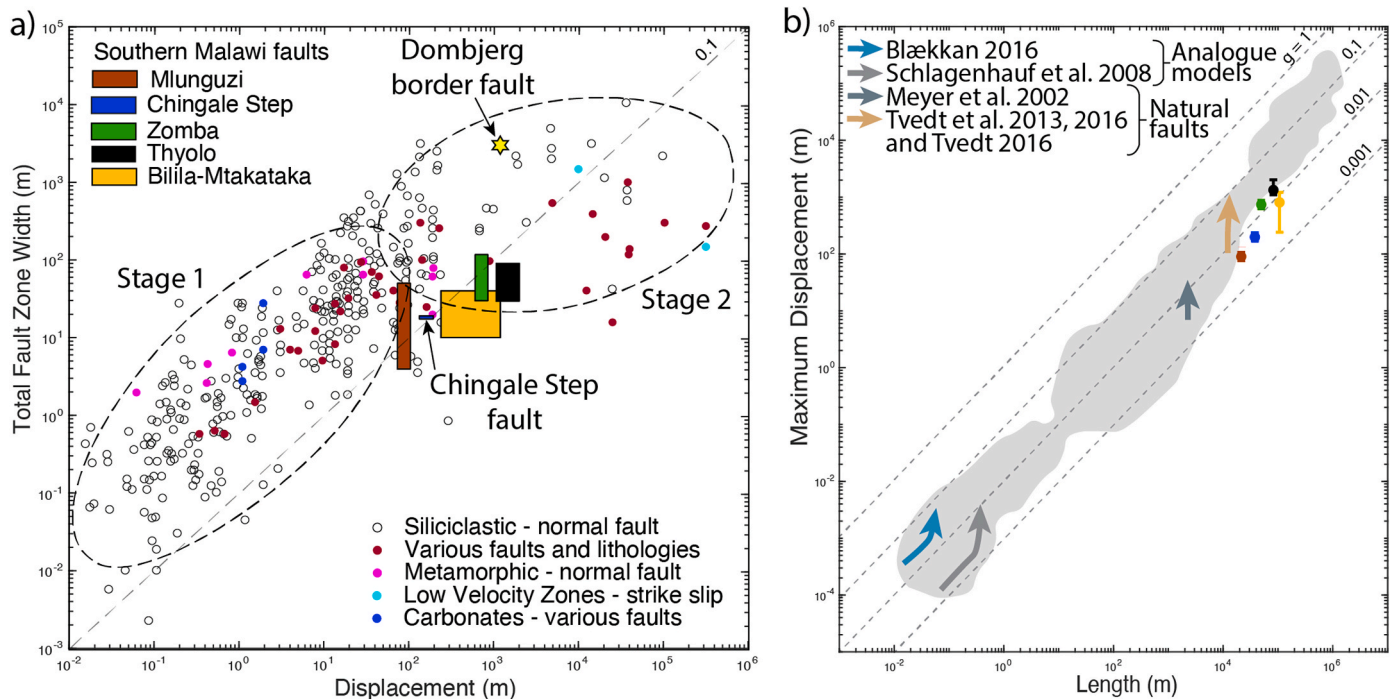


Fig. 13. a) Comparison of Zomba Graben fault zone width-displacement scaling relationships with global data compilation from Torabi et al. (2020) and references therein. Previously studied southern Malawi Bilila-Mtakataka intrarift (Hodge et al., 2018; Williams et al., 2022a) and Thyolo border (Wedmore et al., 2020b) faults are plotted, as is Dombjerg border fault (Kristensen et al., 2016). Two stages of fault growth suggested by Torabi et al. (2020) are annotated, where displacement accrues relatively less damage in faults with >100 m displacement. Zomba Graben faults have narrow fault zone widths for their displacement, compared to mean expected values. b) Comparison of Zomba Graben maximum displacement-length scaling relationships with normal fault global data compiled by Rotevatn et al. (2019). All three Zomba Graben faults have lengths greater than expected for their displacement, similar to Thyolo (black error bar) and Bilila-Mtakataka (yellow error bar) faults. Annotated arrows indicate fault growth trends implied by data in the original figure (Rotevatn et al., 2019). (For interpretation of the references to colour in this figure legend, the reader is referred to the Web version of this article.)

implication of this hypothesis is that there is no footwall exhumation during normal fault slip, and this is contrary to what is commonly observed (Stein and Barrientos, 1985; Parry and Bruhn, 1987; Muirhead et al., 2016) and to numerical modelling (Olive et al., 2014). Hence, we consider that these fault zone width estimates are representative of the wall rock deformation that has progressively accumulated in these fault zones.

In total, we have used 5 transects to constrain the width of 3 fault zones. Although data collected from the same fault are consistent with one another, and we have avoided sites where fault zones may be anomalously wide or narrow (e.g. fault steps and tips, locations where fault displacements are unusually high or low, Figs. 3 and 4), there may still be along-strike changes in the width of these faults that we have not accounted for. Nevertheless, the observation from two other fault zones in southern Malawi that their footwall damage zones are 10–50 m wide (Wedmore et al., 2020b; Williams et al., 2022a), provides confidence that, to the first order, our estimates are representative of the damage accrued by these faults.

7.5. Comparing intrarift and border faults

The border fault (the Zomba fault) has the widest fault zone of the studied faults in the Zomba Graben, and it also has the greatest length and displacement (51 km long, 620–870 m displacement, 32–118 m width; Table 1). Both the Mlunguzi and Chingale Step intrarift faults have damage zone microfracture densities that are less elevated above background protolith values, compared to the Zomba border fault (Fig. 12). Of the intrarift faults, the greater length and displacement Chingale Step fault has damage zone microfracture densities that are more elevated above background values than the Mlunguzi fault. This observation is consistent with the degree of grain fragmentation

increasing with fault displacement: despite the increasing distance from each fault, fragmented clast size decreases from ≤ 1 mm adjacent to the Mlunguzi fault scarp, to ≤ 0.5 mm within 1 m of Chingale Step fault, to fragments 5–100 μm as far as 5 m from the Zomba fault (Fig. 8). The Zomba fault samples 5.2 m from fault show intragranular shattering (Fig. 8d), and may be similar to pulverised rocks and clasts described in other shallow fault zones (Rockwell et al., 2009; Mitchell et al., 2011; Rodríguez-Escudero et al., 2020). In summary, both the spatial extent and intensity of damage (here defined as the elevation of damage zone microfractures above background protolith values) increases from the smaller-length, smaller-displacement Mlunguzi intrarift fault, to the longer, higher-displacement Zomba border fault.

8. Discussion

8.1. Fault displacement-length scaling in the Zomba Graben

Using the Mlunguzi, Chingale Step and Zomba faults, we have been able to constrain the maximum displacement, length, and fault zone width of three active normal faults in a youthful amagmatic continental rift. Evidence that these faults are at an early stage of growth is provided by comparing their maximum displacement-length ratio ($D_{\text{max-L}}$) to the dataset of normal fault scaling compiled by Lathrop et al. (2022). Both the Mlunguzi and Chingale Step intrarift faults are approximately an order of magnitude longer than might be expected for their displacement, with a $D_{\text{max-L}}$ ratio of < 0.006 (Fig. 13). This indicates these faults have been through a phase of fault lengthening with little displacement accrual, which is consistent with early-stage fault zone structural evolution according to ‘constant-length’ (Walsh et al., 2002) or ‘hybrid’ (Rotevatn et al., 2019) models of normal fault growth. This stage is predicted to be followed by a subsequent phase of displacement accrual

and segment linkage with little to no further lengthening. Indeed, there is evidence for relatively recent segment linkage across the Chingale Step fault from detailed geomorphic analysis of its scarp and footwall knickpoints (Wedmore et al., 2020a). In comparison, the Zomba border fault has a D_{\max} -L ratio between 0.01 and 0.015, comparable to the low end of the compiled global dataset for faults longer than 10 km. This may suggest it may already be close to its maximum length, with any subsequent displacement accrual to be accompanied by relatively modest tip propagation.

8.2. Fault zone width and displacement scaling in the Zomba Graben and implications for crustal fluid flow

With fault zone widths of 4–52, 18–20 and 32–118 m, for the Mlunguzi, Chingale Step and Zomba faults, respectively, each fault zone is relatively narrow compared to global fault datasets compiled by Torabi et al. (2020; Fig. 13a). While we can only provide damage zone widths to the accuracy determined by the nature of our sampling, given the absolute microfracture densities and degree of grain fragmentation between each fault, our preferred interpretation is that the higher displacement Zomba border fault has a wider damage zone than the Zomba Graben's intrarift faults. Fault core development is only observed in the Chingale Step transect (1–2 m wide cataclasite and fault gouge), however the absence of fault core in the Mlunguzi and Zomba fault transects may be an observational constraint caused by the semi-continuous nature of exposure and/or erosive processes.

Within zones of localised fluid flow in fault damage zones and fault cores, mineralisation and fluid-rock interaction above background levels can be expected, resulting in the formation of a chemical alteration zone (Sutherland et al., 2012; Kristensen et al., 2016). Across the studied Zomba Graben faults, the chemical alteration zone is expressed by the presence of 1–10 % smectite in all fault core and damage zone samples (Fig. 7), and calcite veining within 1 m of both the Mlunguzi and Chingale Step faults. In all three transects, smectite mineralisation is distributed at the sample scale and linked to the fracture networks associated with each fault, present either within fractures, exploiting grain boundaries (Fig. 8e), or as the alteration product of amphibole (Fig. 8f). This suggests smectite growth is closely linked to local grain comminution and fracture opening during and/or following fault movement, with insufficient subsequent strain to form interconnected, foliated smectite networks. Smectite mineralisation in these fault zones would likely have been promoted by hydrous retrograde reactions between the wall rock and Na^+ and Ca^{2+} rich meteoric fluids that circulate in Malawi's crust to depths of 2–3 km, and whose pathways have been proposed to be controlled by faults (Dulanya et al., 2010; Dávalos-Elizondo et al., 2021). Near-surface smectite growth in these fault zones is also supported by its stability at temperatures < 120–150 °C (Pytte and Reynolds, 1988), which implies growth at < 6 km depth, given an estimated mean geothermal gradient for Malawi Rift of 25–27 °C/km (Njinju et al., 2019).

The spatial extent and intensity of mineralisation in Zomba Graben fault zones is minimal compared to alteration observed in magmatic sections of the East African Rift System. For example, extensive Fe-oxide and jarosite mineralisation is observed along the Bwamba border fault in Uganda (Hollinsworth et al., 2019). Products of extensive fluid-rock interactions are also observed around other examples of basin-bounding border faults, such as the Dombjerg fault in Greenland, where extensive calcite mineralisation occurs within a chemical alteration zone up to 1 km wide (Kristensen et al., 2016). Further qualitative evidence for limited mineralisation and fault healing in the Zomba Graben comes from the incohesive nature of damage zone samples in the field, relatively minor variation in bulk mineralogy (Fig. 7), and observations of open, barren damage zone microfractures (Figs. 9–11).

None of the faults in this study have hosted moderate or large earthquakes in the ~ 150-year written historical record in southern Malawi, and low (~ 0.7 mm/yr; Wedmore et al., 2021) regional

extension rates imply long (10^3 – 10^4 years) earthquake recurrence intervals (Hodge et al., 2015; Williams et al., 2021). In warm, hydrous crust, these timescales may be sufficient for extensive fault zone healing and mineralisation to occur (Morrow et al., 2001; Bosl and Nur, 2002; Kitagawa et al., 2007; Sutherland et al., 2012; Williams et al., 2017; Yehya and Rice, 2020). However, the crust in southern Malawi is relatively cool and thick (~ 45 km; Nyblade and Langston, 1995; Fagereng, 2013; Njinju et al., 2019; Craig et al., 2021; Stevens et al., 2021; Sun et al., 2021) and has been dehydrated by previous high grade metamorphic events (Laó-Dávila et al., 2015; Manda et al., 2019). Furthermore, earthquake sequences in Malawi are shown to be consistent with Coulomb stress changes, without requiring fluid migration (Fagereng, 2013; Gaberty et al., 2019). Negligible fault healing observed within the Zomba Graben is also similar to studies elsewhere in the Malawi Rift (Wedmore et al., 2020b), and may suggest that the presence of a shallow fault-controlled hydrothermal system (Dulanya, 2017; Njinju et al., 2019; Dávalos-Elizondo et al., 2021) is very localised or chemical potential gradients are too small for void-filling precipitates to form from hydrothermal fluids.

8.3. Mechanisms for long faults with narrow fault zones in southern Malawi

To summarise, faults in the Zomba Graben have lengthened quickly, relative to their displacement, while developing only narrow fault zones. Recent studies of other border and intrarift faults in southern Malawi reveal scaling relationships like those observed in the Zomba Graben, with low D_{\max} -L ratios (< 0.005–0.02) and narrow fault zones given their displacement (Hodge et al., 2018; Wedmore et al., 2020b; Ojo et al., 2022a; Williams et al., 2022a, Fig. 13a). This suggests that a common factor may control the growth of faults in southern Malawi.

Given the lack of studies that have tried to relate normal fault displacement-length scaling with normal fault displacement-width scaling, the narrow damage zones we observe in the Zomba Graben may be a typical feature of normal faults during their early stage of growth. Without more field data from active low displacement normal faults, or a fracture mechanics model that can account for rapid normal fault lengthening, it is difficult to evaluate this point further. Below, we have identified three non-mutually exclusive factors that may explain our observations: lithology, fault zone healing, and pre-existing crustal weaknesses.

A large proportion of the global dataset that compares fault displacement and fault zone width in Fig. 13a comprise studies from faults in siliciclastic sedimentary rocks, rather than crystalline igneous or metamorphic rocks such as those present in the Zomba Graben. This could be important for comparisons with normal faults forming in high porosity sandstones, which accrue damage through strain hardening deformation bands (e.g., Shipton and Cowie, 2003). In addition, the relatively stiff metamorphic and igneous rocks in southern Malawi may contribute to the low displacement to length ratio of its faults (Lathrop et al., 2022). However, Torabi et al. (2020) note that lithology does not seem to influence the spread of fault zone width-displacement data at log-log scale, and Savage and Brodsky (2011) find that fault zone thickness shows minimal correlation with lithology. Furthermore, the crystalline basement-hosted Dombjerg border fault (Kristensen et al., 2016) has a disproportionately wide footwall fault zone (600 m) compared to the crystalline basement-hosted Zomba border fault (16–59 m), given their respective displacements (3.3 km vs 0.6–0.9 km) (Fig. 13a).

Fault zone widening may reflect fault zone healing between incremental slip events, so that subsequent slip activates new planes and leads to the formation of multiple anastomosing fault cores (Caine et al., 2010; Callahan et al., 2020). Therefore, the relative lack of healing and volumetrically minor, scattered low-temperature clays within the Zomba Graben fault zones (Section 7.2) may mean that any low cohesion slip surfaces are maintained between slip events and repeatedly

- Kitagawa, Y., Fujimori, K., Koizumi, N., 2007. Temporal change in permeability of the Nojima fault zone by repeated water injection experiments. *Tectonophysics* 443 (3–4), 183–192.
- Kolawole, F., Atekwana, E.A., Laó-Dávila, D.A., Abdelsalam, M.G., Chindandali, P.R., Salima, J., Kalindekafu, L., 2018. Active deformation of Malawi rift's north basin Hinge zone modulated by reactivation of preexisting Precambrian Shear zone fabric. *Tectonics* 37 (3), 683–704.
- Kolawole, F., Firkins, M.C., Al Wahaibi, T.S., Atekwana, E.A., Soreghan, M.J., 2021. Rift interaction zones and the stages of rift linkage in active segmented continental rift systems. *Basin Res.* 33 (6), 2984–3020.
- Kristensen, T.B., Rotevatn, A., Peacock, D.C., Henstra, G.A., Midtkandal, I., Grundvåg, S. A., 2016. Structure and flow properties of syn-rift border faults: the interplay between fault damage and fault-related chemical alteration (Dombjerg Fault, Wollaston Forland, NE Greenland). *J. Struct. Geol.* 92, 99–115.
- Kröner, A., Willner, A.P., Hegner, E., Jaeckel, P., Nemchin, A., 2001. Single zircon ages, PT evolution and Nd isotopic systematics of high-grade gneisses in southern Malawi and their bearing on the evolution of the Mozambique belt in southeastern Africa. *Precambrian Res.* 109 (3–4), 257–291.
- Laó-Dávila, D.A., Al-Salmi, H.S., Abdelsalam, M.G., Atekwana, E.A., 2015. Hierarchical segmentation of the Malawi Rift: the influence of inherited lithospheric heterogeneity and kinematics in the evolution of continental rifts. *Tectonics* 34 (12), 2399–2417.
- Lathrop, B., Jackson, C., Bell, R.E., Rotevatn, A., 2022. Displacement/length Scaling Relationships for Normal Faults; a Review, Critique, and Revised Compilation.
- Ma, S., 2009. Distinct asymmetry in rupture-induced inelastic strain across dipping faults: an off-fault yielding model. *Geophys. Res. Lett.* 36 (20).
- Manda, B.W., Cawood, P.A., Spencer, C.J., Prave, T., Robinson, R., Roberts, N.M., 2019. Evolution of the Mozambique Belt in Malawi constrained by granitoid U-Pb, Sm-Nd and Lu-Hf isotopic data. *Gondwana Res.* 68, 93–107.
- Mitchell, T.M., Faulkner, D.R., 2009. The nature and origin of off-fault damage surrounding strike-slip fault zones with a wide range of displacements: a field study from the Atacama fault system, northern Chile. *J. Struct. Geol.* 31 (8), 802–816.
- Mitchell, T.M., Ben-Zion, Y., Shimamoto, T., 2011. Pulverized fault rocks and damage asymmetry along the Arima-Takatsuki Tectonic Line, Japan. *Earth Planet Sci. Lett.* 308 (3–4), 284–297.
- Morrow, C.A., Moore, D.E., Lockner, D.A., 2001. Permeability reduction in granite under hydrothermal conditions. *J. Geophys. Res. Solid Earth* 106 (B12), 30551–30560.
- Mortimer, E., Paton, D.A., Scholz, C.A., Strecker, M.R., Blisniuk, P., 2007. Orthogonal to oblique rifting: effect of rift basin orientation in the evolution of the North basin, Malawi Rift, East Africa. *Basin Res.* 19 (3), 393–407.
- Mortimer, E., Kirstein, L.A., Stuart, F.M., Strecker, M.R., 2016. Spatio-temporal trends in normal-fault segmentation recorded by low-temperature thermochronology: livingstone fault scarp, Malawi Rift, East African Rift System. *Earth Planet Sci. Lett.* 455, 62–72.
- Muirhead, J.D., Kattenhorn, S.A., Lee, H., Mana, S., Turrin, B.D., Fischer, T.P., Kianji, G., Dindi, E., Stamps, D.S., 2016. Evolution of upper crustal faulting assisted by magmatic volatile release during early-stage continental rift development in the East African Rift. *Geosphere* 12 (6), 1670–1700.
- Muirhead, J.D., Wright, L.J., Scholz, C.A., 2019. Rift evolution in regions of low magma input in East Africa. *Earth Planet Sci. Lett.* 506, 332–346.
- Njinju, E.A., Kolawole, F., Atekwana, E.A., Stamps, D.S., Atekwana, E.A., Abdelsalam, M. G., Mickus, K.L., 2019. Terrestrial heat flow in the Malawi Rifted Zone, East Africa: implications for tectono-thermal inheritance in continental rift basins. *J. Volcanol. Geoth. Res.* 387, 106656.
- Nyblade, A.A., Langston, C.A., 1995. East African earthquakes below 20 km depth and their implications for crustal structure. *Geophys. J. Int.* 121 (1), 49–62.
- Ojo, O.O., Ohnhen, L.O., Kolawole, F., Johnson, S.G., Chindandali, P.R., Atekwana, E. A., Laó-Dávila, D.A., 2022a. Under-displaced normal faults: strain accommodation along an early-stage rift-bounding fault in the Southern Malawi Rift. *Front. Earth Sci.* 10.
- Ojo, O., Thomson, S.N., Lao-Davila, D., 2022b. Neogene - quaternary rifting of the southern Malawi rift and linkage to the late carboniferous – early jurassic Shire rift. *Earth Sp. Sci. Open Arch. ESSOAr.* <https://doi.org/10.1002/essoar.10511357.1> (May), 1–58.
- Olive, J.A., Behn, M.D., Malatesta, L.C., 2014. Modes of extensional faulting controlled by surface processes. *Geophys. Res. Lett.* 41 (19), 6725–6733.
- Ota, Y., Chen, Y.G., Chen, W.S., 2005. Review of paleoseismological and active fault studies in Taiwan in the light of the Chichi earthquake of September 21, 1999. *Tectonophysics* 408 (1–4), 63–77.
- Pan, S., Naliboff, J., Bell, R., Jackson, C., 2022. Bridging spatiotemporal scales of normal fault growth during continental extension using high-resolution 3D numerical models. *G-cubed* 23, e2021GC010316. <https://doi.org/10.1029/2021GC010316>.
- Parry, W.T., Bruhn, R.L., 1987. Fluid inclusion evidence for minimum 11 km vertical offset on the Wasatch fault, Utah. *Geology* 15 (1), 67–70.
- Philippon, M., Willingshofer, E., Sokoutis, D., Corti, G., Sani, F., Bonini, M., Cloetingh, S., 2015. Slip re-orientation in oblique rifts. *Geology* 43 (2), 147–150.
- Pytte, A., Reynolds, R., 1988. The thermal transformation of smectite to illite. In: Naeser, N.D., McCulloch, T.H. (Eds.), *Thermal Histories of Sedimentary Basins*. Springer-Verlag, pp. 133–140.
- Ring, U., Betzler, C., 1995. Geology of the Malawi Rift: kinematic and tectono-sedimentary background to the Chiwondo Beds, northern Malawi. *J. Hum. Evol.* 28 (1), 7–21.
- Rockwell, T., Sisk, M., Girty, G., Dor, O., Wechsler, N., Ben-Zion, Y., 2009. Chemical and physical characteristics of pulverized Tejon Lookout granite adjacent to the San Andreas and Garlock faults: implications for earthquake physics. *Pure Appl. Geophys.* 166 (10), 1725–1746.
- Rodríguez-Escudero, E., Martínez-Díaz, J.J., Giner-Robles, J.L., Tsigis, M., Cuevas-Rodríguez, J., 2020. Pulverized quartz clasts in gouge of the Alhama de Murcia fault (Spain): evidence for coseismic clast pulverization in a matrix deformed by frictional sliding. *Geology* 48 (3), 283–287.
- Rotevatn, A., Jackson, C.A.L., Tvedt, A.B., Bell, R.E., Blækkjan, I., 2019. How do normal faults grow? *J. Struct. Geol.* 125, 174–184.
- Savage, H.M., Brodsky, E.E., 2011. Collateral damage: evolution with displacement of fracture distribution and secondary fault strands in fault damage zones. *J. Geophys. Res. Solid Earth* 116 (3). <https://doi.org/10.1029/2010JB007665>.
- Scholz, C.A., Shillington, D.J., Wright, L.J., Accardo, N., Gaherty, J.B., Chindandali, P., 2020. Intrarift fault fabric, segmentation, and basin evolution of the lake Malawi (nyasa) rift, East Africa. *Geosphere* 16 (5), 1293–1311.
- Sibson, R.H., 1977. Fault rocks and fault mechanisms. *J. Geol. Soc.* 133 (3), 191–213.
- Shipton, Z.K., Cowie, P.A., 2003. A conceptual model for the origin of fault damage zone structures in high-porosity sandstone. *J. Struct. Geol.* 25 (3), 333–344.
- Shipton, Z.K., Soden, A.M., Kirkpatrick, J.D., Bright, A.M., Lunn, R.J., 2006. How thick is a fault? Fault displacement-thickness scaling revisited. In: Abercrombie, R. (Ed.), *Earthquakes: Radiated Energy and the Physics of Faulting*. AGU, pp. 193–198.
- Stamps, D.S., Saria, E., Kreemer, C., 2018. A geodetic strain rate model for the East African Rift System. *Sci. Rep.* 8 (1), 1–9.
- Stanton-Yonge, A., Cembrano, J., Griffith, W.A., Jensen, E., Mitchell, T.M., 2020. Self-similar length-displacement scaling achieved by scale-dependent growth processes: Evidence from the Atacama Fault System. *J. Struct. Geol.* 133, 103993.
- Stein, R.S., Barrientos, S.E., 1985. Planar high-angle faulting in the basin and range: geodetic analysis of the 1983 borah peak, Idaho, earthquake. *J. Geophys. Res. Solid Earth* 90 (B13), 11355–11366.
- Stevens, V.L., Sloan, R.A., Chindandali, P.R., Wedmore, L.N., Salomon, G.W., Muir, R.A., 2021. The entire crust can be seismogenic: evidence from southern Malawi. *Tectonics* 40 (6), e2020TC006654.
- Sun, M., Gao, S.S., Liu, K.H., Mickus, K., Fu, X., Yu, Y., 2021. Receiver function investigation of crustal structure in the Malawi and Luangwa rift zones and adjacent areas. *Gondwana Res.* 89, 168–176.
- Sutherland, R., Toy, V.G., Townend, J., Cox, S.C., Eccles, J.D., Faulkner, D.R., Prior, D.J., Norris, R.J., Mariani, E., Boulton, C., Carpenter, B.M., 2012. Drilling reveals fluid control on architecture and rupture of the Alpine fault, New Zealand. *Geology* 40 (12), 1143–1146.
- Torabi, A., Berg, S.S., 2011. Scaling of fault attributes: a review. *Mar. Petrol. Geol.* 28 (8), 1444–1460. <https://doi.org/10.1016/j.marpetgeo.2011.04.003>.
- Torabi, A., Ellingsen, T.S.S., Johannessen, M.U., Alaei, B., Rotevatn, A., Chiarella, D., 2020. Fault zone architecture and its scaling laws: where does the damage zone start and stop? *Geological Society, London, Special Publications* 496 (1), 99–124.
- Walsh, J.J., Watterson, J., 1988. Analysis of the relationship between displacements and dimensions of faults. *J. Struct. Geol.* 10 (3), 239–247.
- Walsh, J.J., Nicol, A., Childs, C., 2002. An alternative model for the growth of faults. *J. Struct. Geol.* 24 (11), 1669–1675.
- Walshaw, R.D., 1965. The geology of the nchue-balaka area. *Bull. Geol. Soc. Malays.* 19.
- Wedmore, L.N.J., Biggs, J., Williams, J.N., Fagereng, Å., Dulanya, Z., Mphepo, F., Mdala, H., 2020a. Active fault scarps in southern Malawi and their implications for the distribution of strain in incipient continental rifts. *Tectonics* 39 (3), e2019TC005834.
- Wedmore, L.N., Williams, J.N., Biggs, J., Fagereng, Å., Mphepo, F., Dulanya, Z., Willoughby, J., Mdala, H., Adams, B.A., 2020b. Structural inheritance and border fault reactivation during active early-stage rifting along the Thyolo fault, Malawi. *J. Struct. Geol.* 139, 104097.
- Wedmore, L.N., Biggs, J., Floyd, M., Fagereng, Å., Mdala, H., Chindandali, P., Williams, J.N., Mphepo, F., 2021. Geodetic constraints on cratonic microplates and broad strain during rifting of thick Southern African lithosphere. *Geophys. Res. Lett.* 48 (17), e2021GL093785.
- Wessel, B., Huber, M., Wohlfart, C., Marschalk, U., Kosmann, D., Roth, A., 2018. Accuracy assessment of the global TanDEM-X digital elevation model with GPS data. *ISPRS J. Photogrammetry Remote Sens.* 139, 171–182.
- Wibberley, C.A., Shimamoto, T., 2003. Internal structure and permeability of major strike-slip fault zones: the Median Tectonic Line in Mie Prefecture, Southwest Japan. *J. Struct. Geol.* 25 (1), 59–78.
- Williams, J.N., Toy, V.G., Smith, S.A., Boulton, C., 2017. Fracturing, fluid-rock interaction and mineralisation during the seismic cycle along the Alpine Fault. *J. Struct. Geol.* 103, 151–166.
- Williams, J.N., Fagereng, Å., Wedmore, L.N., Biggs, J., Mphepo, F., Dulanya, Z., Mdala, H., Blenkinsop, T., 2019. How do variably striking faults reactivate during rifting? Insights from southern Malawi. *G-cubed* 20 (7), 3588–3607.
- Williams, J.N., Mdala, H., Fagereng, Å., Wedmore, L.N., Biggs, J., Dulanya, Z., Chindandali, P., Mphepo, F., 2021. A systems-based approach to parameterise seismic hazard in regions with little historical or instrumental seismicity: active fault and seismogenic source databases for southern Malawi. *Solid Earth* 12 (1), 187–217.
- Williams, J.N., Fagereng, Å., Wedmore, L.N., Biggs, J., Mdala, H., Mphepo, F., Hodge, M., 2022a. Low dissipation of earthquake energy where a fault follows pre-existing weaknesses: field and microstructural observations of Malawi's bilila-mtakataka Fault. *Geophys. Res. Lett.* 49 (8), e2021GL095286.
- Williams, J.N., Wedmore, L.N.J., Scholz, C.A., Kolawole, F., Wright, L.J.M., Shillington, D.J., et al., 2022b. The Malawi Active Fault Database: an onshore-offshore database for regional assessment of seismic hazard and tectonic evolution. *G-cubed* 23, e2022GC010425. <https://doi.org/10.1029/2022GC010425>.
- Wilson, J.E., Chester, J.S., Chester, F.M., 2003. Microfracture analysis of fault growth and wear processes, Punchbowl Fault, San Andreas system, California. *J. Struct. Geol.* 25 (11), 1855–1873.

Wintsch, R.P., Christoffersen, R., Kronenberg, A.K., 1995. Fluid-rock reaction weakening of fault zones. *J. Geophys. Res.: Solid Earth* 100 (B7), 13021–13022.

Wright, L.J., Muirhead, J.D., Scholz, C.A., 2020. Spatiotemporal variations in upper crustal extension across the different basement terranes of the Lake Tanganyika Rift, East Africa. *Tectonics* 39 (3).

Yang, Z., Chen, W.P., 2010. Earthquakes along the East African Rift System: a multiscale, system-wide perspective. *J. Geophys. Res.* 115, B12309.

Yehya, A., Rice, J.R., 2020. Influence of fluid-assisted healing on fault permeability structure. *J. Geophys. Res. Solid Earth*, e2020JB020553.